

GARNER VALLEY DOWNHOLE ARRAY OF ACCELEROMETERS: INSTRUMENTATION AND PRELIMINARY DATA ANALYSIS

BY RALPH J. ARCHULETA, SANDRA H. SEALE, PETER V. SANGAS,
LAWRENCE M. BAKER AND SCOTT T. SWAIN

ABSTRACT

The Garner Valley downhole array (GVDA) in southern California (33°41.60'N, 116°40.20'W) is a five-element array of three-component, dual-gain force balance accelerometers that are capable of measuring accelerations from 3×10^{-6} to 2.0 g over a frequency range from 0.0 to 100 Hz. The accelerometers are placed at depths of 0, 6, 15, 22, and 220 m. The lithostratigraphy is 19 m of soil overlying a 24-m layer of weathered granite below which is granite (tonalite). The array, only 7 km from the San Jacinto fault, is located at the northern end of the Anza seismic gap on the San Jacinto fault, where an M 6.5 or greater earthquake can be expected. It is only 35 km from the Indio segment of the San Andreas fault, which last ruptured with an $M > 8$ earthquake around 1700 A.D. From its installation in July 1989 through July 1991, GVDA has recorded 280 earthquakes with magnitudes ranging from 1.2 to 4.7 and epicentral distances ranging from 0 to 110 km. The maximum acceleration recorded was 89 cm/sec² from an M_L 4.2 earthquake 15.8 km (hypocentral distance) from GVDA. The average amplification of the apparent seismic moment between 220-m depth and the surface is about 13 for over five orders of magnitude in the size of the recorded earthquakes. The spectral ratio 0/220 of horizontal acceleration amplitude spectrum shows a mean amplification of about 10 for the frequency range of 2.0 to 30 Hz for 17 events. Resonance peaks exist at about 1.7, 3.0, and 12.0 Hz where the spectral ratio 0/220 is nearly 40. Analysis of the acceleration spectra of two specific earthquakes that have nearly the same hypocenter but with different magnitudes, M 4.2 and 2.5, shows that the weathered granite zone, beneath the soil, strongly attenuates the spectral amplitudes for frequencies greater than 40 Hz. The impedance of the soil relative to the weathered granite amplifies all frequencies by about a factor of 3, leading to spectral levels that are greater at the surface than at 22-m depth, near the top of the weathered granite. The acceleration spectra at each depth show resonant peaks at the same frequencies. The spectra at each depth are well correlated for both earthquakes. The acceleration spectrum at 220 m is nearly constant for frequencies less than 60 Hz, which implies that there is little or no attenuation.

INTRODUCTION

As more ground-motion data are collected, the local geological site condition appears to be the dominant factor for controlling the variation in ground motion (e.g., Roger *et al.*, 1985; Mueller, 1986; Aki, 1988). A site effect can cause very different behavior in the time history of the ground motion. The accelerograms in Mexico City from the 1985 Michoacán, Mexico, earthquake clearly demonstrate the influence of the ancient lakebed sediment sites with resonant amplifications of 40 or more (Singh *et al.*, 1988). Using accelerograms from the 1971 San Fernando, California, earthquake, Liu and Heaton (1984) showed how the San Fernando and Los Angeles basins produced long trains of surface waves while the mountain sites recorded high-frequency short-duration pulses as

waves propagated from the San Fernando valley across the Santa Monica mountains into the Los Angeles basin. The accelerograms from the 1985 Valparaiso, Chile, earthquake vary both in amplitude and duration depending on whether the accelerometer was on a hard rock or sediment site (Çelebi, 1987). The site effect was emphasized once more in the 1989 Loma Prieta, California, earthquake, where soft sediment sites showed resonant amplifications of a factor of 20 or more compared to hard-rock sites (Housner, 1990), while amplifications due to impedance contrasts were about a factor of 3.

Even though the consequences are most dramatic in the cases of strong motion, the site effect, of course, exists for any level of shaking. For accelerations of 10^{-5} to 10^{-3} g, King and Tucker (1984) found spectral amplification factors of 5 to 10 over distances of 100 m by comparing ground motions at the edge and within a sediment-filled valley. Similar spectral amplification factors of 2.5 to 4 were found by comparing aftershocks of the 1984 Coalinga, California, earthquake recorded on bedrock and alluvial sites (Mueller, 1986; Jarpe *et al.*, 1988). Because both sites are at the surface, the factor of 2 due to the stress-free condition is not included. It appears that spectral amplifications around 2.5 to 4 are the norm when comparing a surface bedrock site to a surface alluvial site (for additional references, see Aki, 1988, and Rogers *et al.*, 1985).

Attenuation and amplification are both relative measurements in that they are measured with respect to some baseline. The baseline record is generally taken to be a hard-rock site, where the effects of either attenuation or amplification are assumed to be minimized. In order to isolate the effects due to site conditions from those of the source or path, a common practice is to produce a spectral ratio by dividing the amplitude spectrum of the soil site by the amplitude spectrum of the rock site. Basic questions arise in deciding which rock site to select. Is the rock site near? Does it show large variations in its spectra? The optimum situation occurs when the rock site is directly below the surface site and much deeper than the local geological conditions to be studied; in other words, it produces a downhole recording of the ground motion before it is affected by the local site geology (Joyner *et al.*, 1976, Johnson and Silva, 1981; Archuleta, 1986; Malin *et al.*, 1988; Seale and Archuleta, 1989; Fletcher *et al.*, 1990; Cramer and Real, 1990; Blakeslee and Malin, 1991; Aster and Shearer, 1991a, 1991b). The obvious extension of a single sensor located below and deeper than the local geological strata is a vertical array of sensors between the surface and the deepest sensor that examine how seismic waves are attenuated and amplified as they propagate to the surface.

Amplification due to the impedance contrast between two materials is a result of the conservation of energy (Carter *et al.*, 1984). Assuming complete transmission the amplification factor for a plane wave traveling from a material with velocity v_1 and density ρ_1 into a material with velocity v_2 and density ρ_2 is

$$A = \sqrt{\frac{v_1 \rho_1}{v_2 \rho_2}}.$$

Although this type of amplification is frequency independent, it is wavelength dependent (Bullen, equation 10, p. 128, 1963). For example, with a layer over a half-space, when the wavelength is much larger than the thickness of a layer,

the amplification is only that of the free surface (Shearer and Orcutt, 1987). The impedance amplification is also finite, being proportional to the ratio of two finite quantities, but might still be very large (around 3 to 4) if the near-surface material velocity is low. Of course, the free surface will multiply this amplification by a factor of 2 for wavelengths shorter than the layer thickness.

Resonances amplify traveling plane waves in a different way. The amplification due to resonances is frequency dependent. The amplification can be very large at certain frequencies; theoretically, infinite in the absence of material damping. The effect of resonances is well documented: the 1985 Michoacán, Mexico, earthquake (M_S 8.1) (Anderson *et al.*, 1986; Çelebi *et al.*, 1987; Singh *et al.*, 1988); the 1986 Chalfant Valley, California, earthquake (M_L 6.4) (Seale and Archuleta, 1989); and the 1989 Loma Prieta, California, earthquake (Housner, 1990). Under ideal, or nearly ideal, conditions, such as a horizontally layered velocity structure, the amplification of seismic waves is routinely computed when the velocity structure is known (e.g., Silva, 1976; Cranswick *et al.*, 1985; Seale and Archuleta, 1989). Fortunately, determining the velocity structure is relatively straightforward and generally determined from data independent of the data being analyzed. For example, velocity structure may be determined from reflection experiments or direct logging of boreholes (Beeston and McEvelly, 1977; Liu *et al.*, 1988).

Opposing the amplification of seismic waves is attenuation. Determining the attenuation structure at a site is not straightforward. Most often the attenuation structure is not independently determined from the data one wishes to interpret. Just as the velocity structure has different values for compressional and shear waves, so too does the attenuation. Thus compressional waves and shear waves must be analyzed separately. Attenuation for each wave type is generally described by a single parameter, Q , the quality factor, through the relation

$$A = A_0 e^{-\pi ft/Q}, \quad (1)$$

where A_0 is the initial amplitude, f is frequency of the wave, and t is the time a wave has spent in the region with quality factor Q .

The interpretation of the time t is critical in determining a quality factor Q . If one assumes that there is only one value of Q for the entire travel path, the time can be interpreted as the travel time between source and receiver. However, if the medium has different values of Q for different parts of the travel path, the interpretation of Q is not unique; the attenuation is linked to the velocity structure through the time variable. Although Q may be a function of position, the net effect is still represented by the ratio t/Q , referred to as t^* (nomenclature for regional or teleseismic seismograms) or κ (for locally recorded seismograms or accelerograms; Anderson and Hough, 1984). Anderson and Hough (1984) provided a critical interpretation of κ . They assumed that κ is comprised of two principal parts of the propagation path: one part that is due primarily to the horizontal travel path κ_R and the other part of the path that is due primarily to the vertical travel path κ_0 . This separation of κ leads to a natural conclusion. Namely, κ_R is the attenuation experienced by the body waves as they travel through the crustal rocks, while κ_0 is the attenuation due to the local site geology. Recent studies of κ show that it is dominated by κ_0 (Lindley *et al.*, 1987; Hough and Anderson, 1988; Frankel and Wennerberg,

1989; Seale and Archuleta, 1989; Fletcher *et al.*, 1990, Aster and Shearer, 1991b; Lindley and Archuleta, 1992). The direct implication of this result is that Q must be high (approximately 800 to 1000) for crustal rocks.

This has important consequences for ground motion and particularly the amplitude spectrum. Assuming that the time series is dominated by body waves and the near-surface geology is nearly the same from station to station, the shape of the amplitude spectrum will show almost no variation with distance although the absolute level will decrease with increasing distance due to geometrical attenuation. Thus one could interpret the constancy of the spectral shape as implying that Q is directly proportional to frequency, $Q = Q_0 f$ (e.g., Console and Rovelli, 1981). Suppose one substitutes $Q = Q_0 f$ into the attenuation relation (equation 1); the attenuation is no longer

$$A = A_0 e^{-\pi f t / Q} = A_0 e^{-\pi f t / (Q_0 f)} = A_0 e^{-\pi t / Q_0} \quad (2)$$

frequency dependent but is dependent only on the travel time t of the wave and Q_0 . A critical underlying assumption is that the value of Q_0 applies for the entire travel time from source to site. The key observation that the spectral shape is nearly the same from site to site can be explained by having attenuation dominated by the local site condition, in which case the travel time and Q apply only to the vertical part of the travel path, not to the whole path. Recent analysis of local site attenuation shows that the local site Q is constant or proportional to an inverse power of frequency (Frankel and Wennerberg, 1989; Boatwright *et al.*, 1991; Lindley and Archuleta, 1992).

Estimating the effect of the local site geology presents a natural dilemma. On one hand, materials characterized by slow wave speeds and low densities support amplification and resonances. On the other hand, these material properties are associated with large damping or low Q . In fact, these materials are those most likely to show nonlinear damping (Seed and Idriss, 1970, Sun *et al.*, 1988). Thus, local site geology consisting of soft soil overlying hard rock simultaneously supports two opposing phenomena: amplification and attenuation. Quantifying the relative contribution of these competing factors is the basic purpose of the Garner Valley, California, downhole array (GVDA).

GARNER VALLEY DOWNHOLE ARRAY (GVDA)

Location

The site for a vertical array of strong-motion accelerometers was selected with three basic criteria in mind. First, it had to be in a seismically active area that would produce both strong and weak ground motion. Second, it had to be in an area where there existed good local control on the location of earthquakes. Third, the site had to be one where soil, with minimum thickness of 15 to 20 m, overlay hard rock. These criteria were satisfied at Garner Valley, California (Fig. 1). The Garner Valley downhole array (33°41.60'N, 116°40.20'W) is only 7 km off the trace of the San Jacinto fault, the most active strand of the San Andreas fault system in southern California, and only about 35 km from the San Andreas fault itself. It is situated at the northern end of the Anza seismic gap (Thatcher *et al.*, 1975). This section of the San Jacinto fault has accumulated at least 1.1 m of slip since the 1899 earthquake, leaving the possibility of an M 6.5 to 7.0 earthquake in the near future (Rockwell *et al.*, 1990). GVDA is

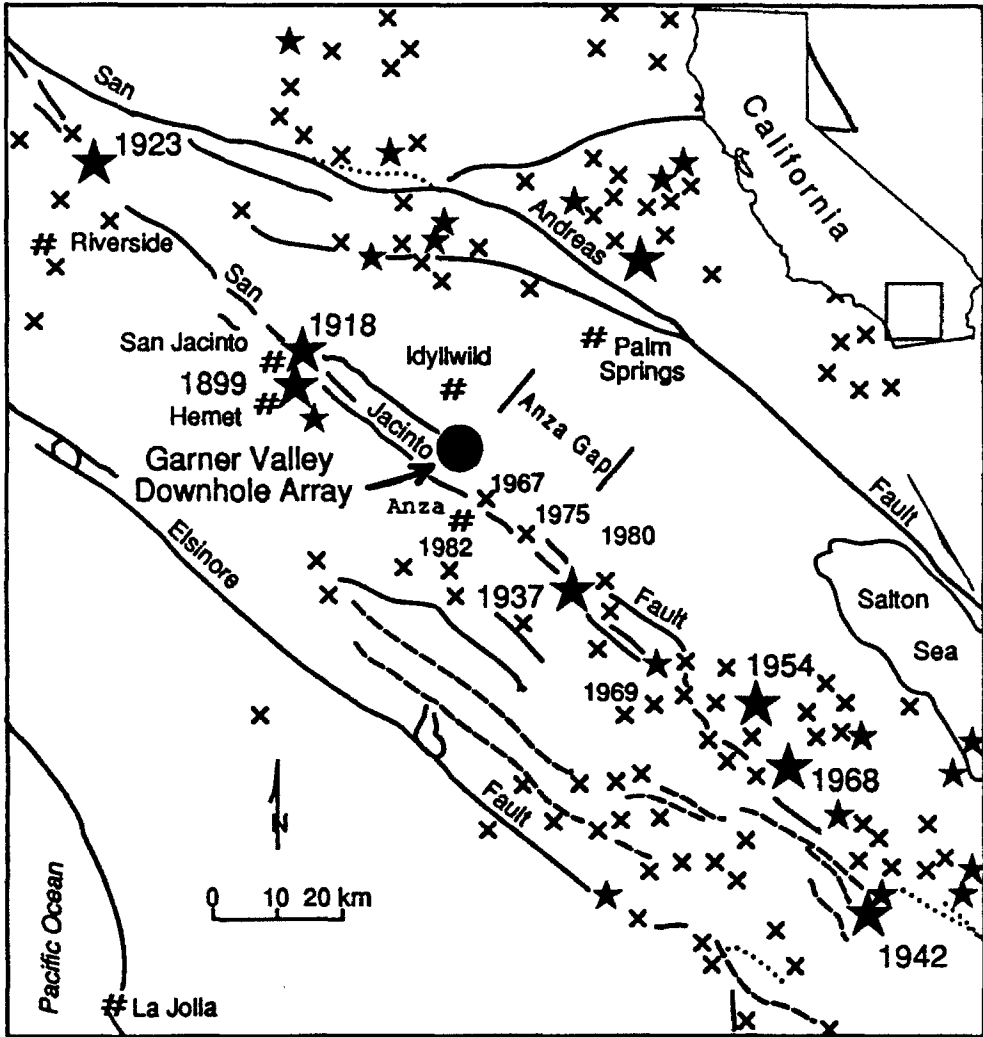


FIG. 1. Seismicity (1932 to 1982) for magnitudes greater than 4.0 and faults in the region surrounding the Garner Valley downhole array. Map area is the square region outlined in the inset map of the state of California, shown in the upper right corner. The symbols for the seismicity are M 4 to 5 (\times), M 5 to 6 (\star), and M 6-7 (\star). (Modified from Sanders and Kanamori, 1984.)

only 35 km from the Indio segment of the San Andreas fault; this segment last ruptured about 1680 ± 40 A.D. with a great earthquake (Sieh *et al.*, 1989).

Small earthquakes ($M > 1.5$) occur regularly, with about 10 earthquakes recorded monthly at GVDA. The Anza seismic gap has been the focal point since 1983 of a joint study by the Institute of Geophysics and Planetary Physics (IGPP) at UC San Diego and the USGS. Consequently, these two groups have put in a 10-station array of velocity transducers with digital recording (Berger *et al.*, 1984; Fletcher *et al.*, 1987) and two borehole installations with velocity transducers in bedrock (Fletcher *et al.*, 1990). This specialized array of recorders coupled with the USGS Southern California Network of high-gain velocity transducers provide excellent coverage of the nearby and surrounding area. All magnitudes are provided by the USGS Southern California Network.

The GVDA site is in a shallow valley within the southern California igneous batholith (Hill, 1981). It is within an ancestral lakebed that is presently the site of extensive deposition of fine materials derived from both the crystalline rocks and from dissection of the older alluvial deposits (Hill, 1981). Drilling and coring by the Army Corps of Engineers show that the soil is comprised of fine alluvial and granular silty sands, silts, and some clay layers (R. Ledbetter, 1989, written comm.). These deposits overlie granitic rocks that are dominantly hornblende tonalite (Hill, 1981). Velocity logs taken by the USGS (Gibbs, 1989) (Fig. 2) show an 18-m-thick layer with an average shear-wave speed of about 220 m/sec. The upper 18 m of soil has been analyzed in detail using geotechnical methods (Pecker and Mohammadioun, 1991). Their findings are shown in Table 1. The value of 2000 m/sec depths greater than 22 m is arbitrary and does not affect their basic results for the shallower depths (A. Pecker, 1991, personal comm.). For depths above 18 m, the geotechnical results are similar to those of Gibbs, if one assumes that Figure 2 represents an average velocity structure marking only the major changes in the velocity. Below this soil layer is a layer of weathered granite for which Gibbs finds a shear wave speed of 580 m/sec extending to 60 m. Having reexamined the original record sections taken by Gibbs, we would place the velocity step from 580 to 1310 m/sec around 40 to 45 m, a depth more consistent with the short-baseline refraction survey (R. Ledbetter, 1989, written comm.). This difference is based on our interpretation of where the first arrivals depart from a straight line. The shear wave speed is 1310 m/sec from this boundary to 100 m, the maximum depth that was logged. Approximately 7 km from GVDA, the USGS operates two borehole stations (KNW) that have velocity transducers installed (Fletcher *et al.*, 1990; Aster and Shearer, 1991a, 1991b). These holes, drilled in similar igneous rocks but without any sediment cover, show a shear-wave velocity of 2650 m/sec below 50 m.

Accelerometers and Data Acquisition

Because one of the primary objectives is to compare strong motion and weak motion, we had Kinometrics modify its standard three-component downhole force balance accelerometer (FBA-13DH) to produce a dual-gain accelerometer: two output channels for each component of motion. The low-gain channel is a standard FBA with a maximum 2 *g* acceleration; the high-gain channel has peak acceleration of 0.1 *g*. The low-gain channel has a flat amplitude response to acceleration from 0.0 to 100 Hz, at which frequency the response drops off at 12 dB/octave. The high-gain channel has a flat amplitude response to acceleration between 0.025 and 100 Hz. We highpass filtered the high-gain channel to avoid having a DC response that could saturate the digitizer from even the slightest amount of tilting. The low-frequency limit of 0.025 Hz is not a concern, because most small earthquakes that will be recorded on the high-gain channel do not have durations that exceed 40 sec.

Each channel is digitized with a 16-bit Tustin A/D at 500 samples/sec. A four-pole (24 dB/octave) anti-alias filter at 100 Hz is added to the 12 dB/octave from the accelerometer. Thus after the signal has passed through the entire system the amplitude response decays at 36 dB/octave above 100 Hz. This decay rate coupled with the Nyquist of 250 Hz implies that any signal that folds back to the spectra will be attenuated by at least 72 dB. The 16-bit digitizer allows us to cover accelerations from ± 2.0 to $\pm 6.0 \times 10^{-5}$ *g* on the low-gain

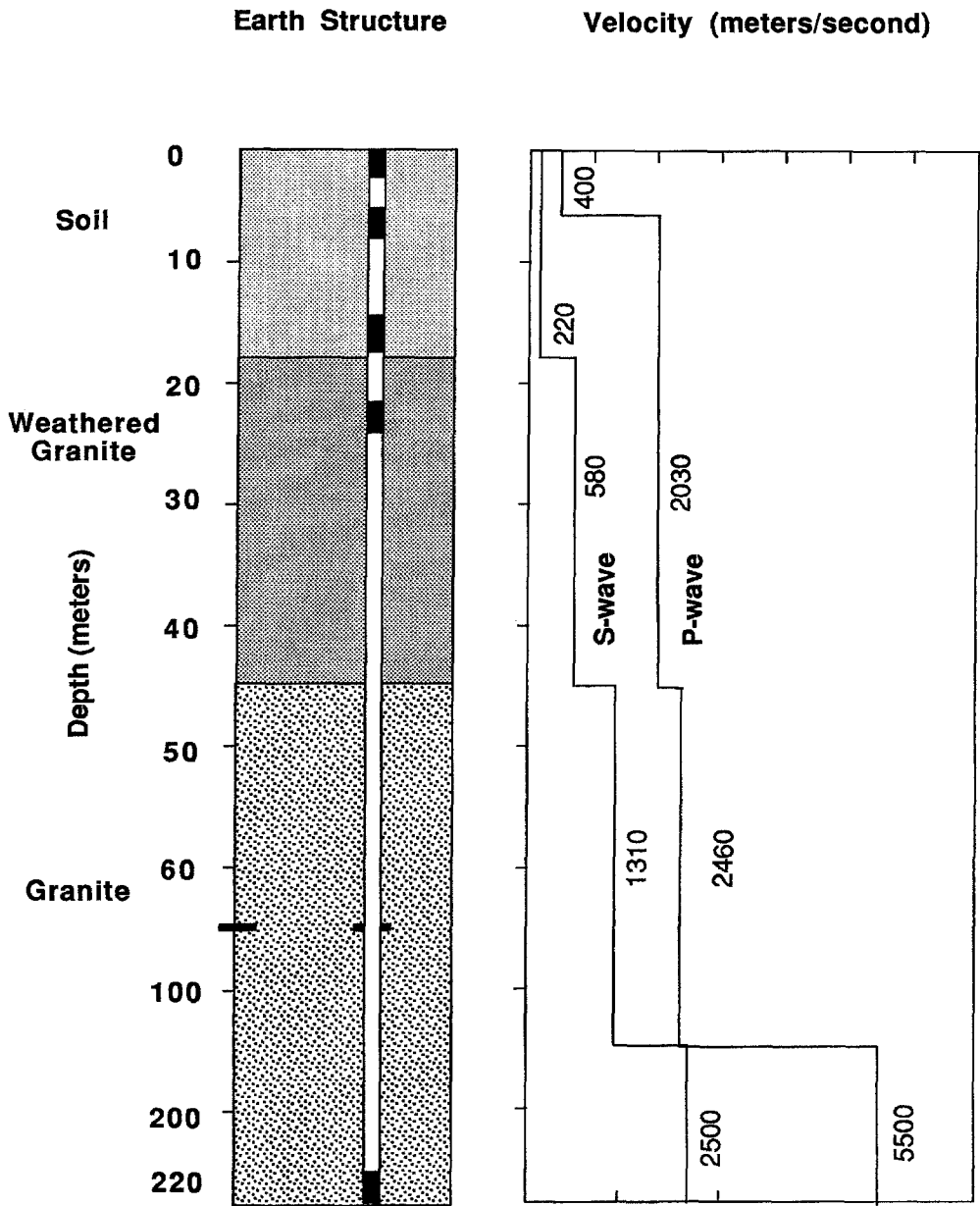


FIG. 2. Lithology and velocity structure at GVDA. Velocities are based on logs to a depth of 100 m. Granite is a generic term in this figure; the rock is hornblende tonalite (Hill, 1981).

channel, and from ± 0.1 to $\pm 3 \times 10^{-6} g$ on the high-gain channel with 64 dB overlap between the two channels (Fig. 3). This 64-dB overlap guarantees that if the high-gain channel saturates, the signal-to-noise on the low-gain channel will be at least 1584. Absolute time from a GOES satellite is injected into this data stream, which is analyzed on a Digital Equipment Corporation (DEC) VAX Workstation II. The data acquisition system receives power from an uninterruptible power supply (UPS) with a capacity of 5 hours. The computer system is

TABLE 1
VELOCITY STRUCTURE AND DENSITY*

Depth (m)	Shear-Wave Velocity (m/sec)	Density (gm/cm ³)
0-1	90	1.95
1-2	130	1.95
2-4	165	2.0
4-6	190	2.0
6-8	215	2.0
8-11.5	240	2.0
11.5-15	260	2.0
15-18	280	2.05
18-22	600	2.2
> 22	2000	2.4

* Taken from Pecker and Mohammadioun (1991).

linked to the UCSB by a 9600-baud modem that allows us to query the system (Fig. 4).

A computer algorithm continuously examines the data stream. Using criteria based on the ratio of the short-term average signal level to long-term average signal level, the algorithm decides whether an event has occurred and subsequently stores the data for all of the channels. It stores all of the data following the trigger plus 5 sec of data preceding the trigger. (The exact number of seconds is a parameter set by the operator; 5 sec allows GVDA to record small earthquakes on the San Andreas fault from Banning to Coachella.) This allows the system to record the initial *P* wave as well as the *P*-wave coda and *S* waves that follow. The data initially were written to a TK50 tape, which is retrieved from the site at least once per month; the data are now written to a hard disk, which is dumped to tape once per month. Data acquisition is at the rate of 30,000 bytes per second and will soon go to 60,000 bytes per second with the addition of four surface instruments and one more downhole accelerometer. Total recording time on the hard disk is 142 minutes when all 60 channels are operating.

Accelerometer Placement

There is one surface accelerometer and four downhole accelerometers at depths of 6, 15, 22, and 220 m within a 3 × 3 m area; a fourth downhole accelerometer is planned to be installed at a depth of 43 m. The three individual accelerometer components are stacked vertically and placed in a specially designed two-piece stainless steel cylindrical casing. The stacked accelerometer package is locked inside the casing using a snap ring and a retaining plate (Fig. 5). The steel components that make up the casing are all welded together with low-carbon content rod to minimize carbon precipitation. Each casing is leak tested with helium. The casing is fitted with a high-pressure electrical connector made from glass-reinforced epoxy. The second half of the connector is bonded to the outer jacket of the electrical cable to prevent any water from entering the cable. The bulkhead is screwed into the cylinder and sealed with o-rings, making one continuous waterproof instrument.

Near its top the stainless steel casing is fitted to a gimbal system. Attached to the bottom of the casing is a tapered 30-lb lead weight that assists the

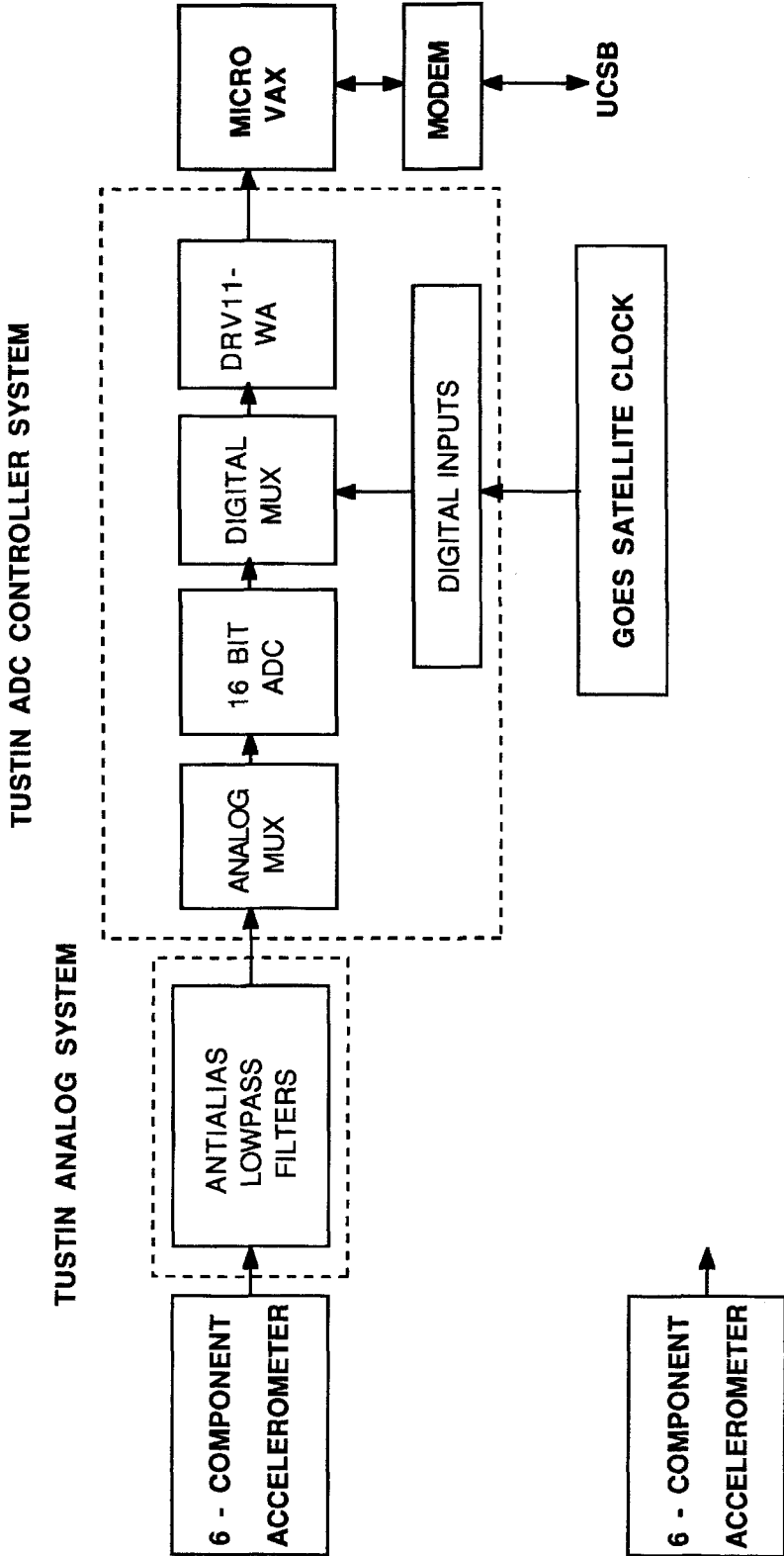


FIG. 4. Block diagram of the data acquisition system at GVDA. A MicroVaxII field computer serves as the data acquisition system. Each of the 30 analog data streams are digitized at 500 s/sec and fed to the computer. The data acquisition is software controlled. Individual system components are discussed in the text.

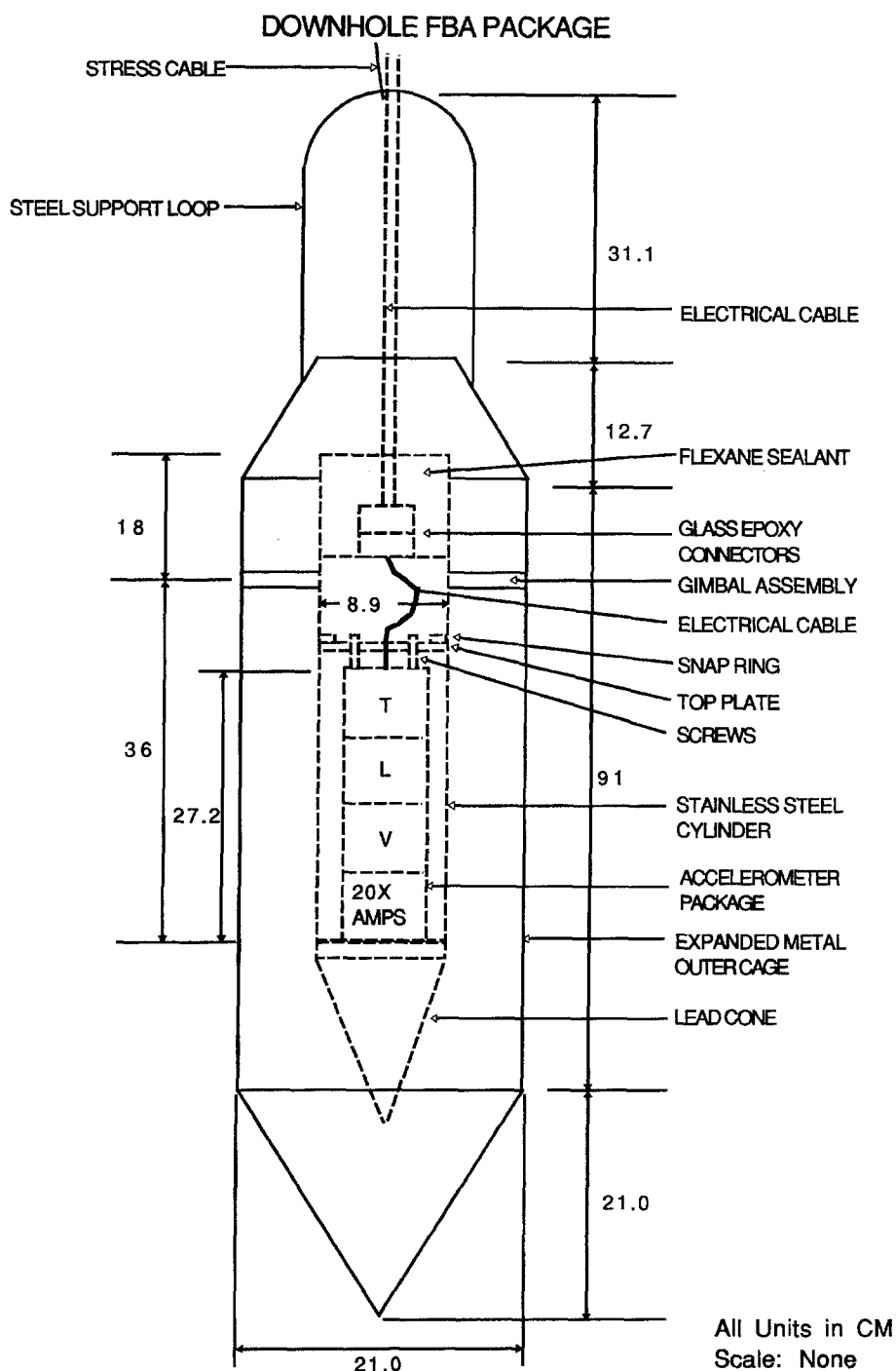


FIG. 5. Diagram of the FBA downhole package. The FBA sensors and electronics are stacked and encased in a stainless steel cylinder that is connected to a gimbal system that allows the FBA to level itself in the hole. The cylinder itself is within an expanded metal cage that protects the instrument during deployment and provides the space for the gimballed cylinder to find local vertical. The electronics in the FBA are connected to the cable through glass epoxy connectors. The volume surrounding the connectors is filled with flexane sealant as an added precaution against water contamination. Dimensions are given in cm, but the figure itself is not drawn to exact scale.

The cable itself is made from several different components. The cable has nine individually shielded twisted pairs plus a strain wire. Each conductor is insulated with polypropylene, and each pair is enclosed in a polyethylene jacket. Both polypropylene and polyethylene have excellent electrical insulating properties, and polyethylene is extremely water resistant. The entire assembly is enclosed in a polyurethane jacket that has excellent water blocking capability and abrasion resistance, which is critical for downhole applications where the cable will be rubbing against the outer side of the hole. The void space within the polyurethane jacket, the region between the twisted pairs, is filled with silicone rubber to prevent water migration inside the cable in the event that the outer jacket is torn.

Once assembled, the entire package (Fig. 5) is lowered into the borehole. When the package is at the right depth, slow-acting cement is pumped into the hole at approximately the same depth as the instrument package. During this period the tilt is monitored by observing the DC acceleration, which has been previously calibrated against degrees of tilt in the laboratory. If the accelerometer package does not come within two degrees of local vertical, the package is retrieved and the placement is restarted. All of the GVDA downhole components are within 2° of local vertical; most are within 0.25° of local vertical. The deployment of the downhole package does not allow determination of the azimuthal orientation of the horizontal components. Using the method described by Aster and Shearer (1991a), we have determined that the 220-m horizontal components are oriented at 170° and 260° clockwise from North.

Another accelerometer will be installed at 43 m, just below the weathered granite interface. To complement the downhole accelerometers we have installed four surface accelerometers (Guralp CMG-5) in a linear array with the existing surface accelerometer. The final configuration at Garner Valley will be five downhole accelerometers and five surface accelerometers, all being three-component and dual-gain. The array will produce 30,000 samples per second when triggered.

DATA AND ANALYSIS

Although the instruments were deployed in June 1989, full operation of the GVDA did not begin until mid-August 1989. From July 1989 through June 1990 280 earthquakes ranging in magnitude from 1.1 to 4.7 have been recorded (Fig. 6). Table 2 provides a list of earthquakes and parameters used in this paper. The maximum acceleration recorded is 89 cm/sec^2 , on the vertical component at the surface from a M 4.2 earthquake (event 8, Table 2) whose hypocenter was 14.5 km deep and 8.6 km from GVDA. The two earthquakes with the greatest magnitudes, M_L 4.7 and M_L 4.6 (events 19 and 20, Table 2), aftershocks of the 28 February 1990, Upland, California, earthquake, are about 110 km from GVDA and outside the boundary of the map. The distribution of earthquakes may be misleading (Fig. 6). The instruments will record M 1.2 earthquakes within 30 km, but obviously will not record such small earthquakes at much greater distances. Thus the large number of small earthquakes near GVDA does not represent the full distribution of earthquakes within the area of the map. However, the distribution of recorded earthquakes does show that GVDA is certainly within a seismically active area where the seismicity of small magnitude earthquakes mirrors the greater magnitude earthquakes (Fig. 1). The Anza seismic gap (Fig. 1) is relatively void of earthquakes even at the magnitude 1 to 2 level.

GARNER VALLEY DOWNHOLE ARRAY

Recorded Earthquakes JULY 1989 - MAY 1991 M > 1.0

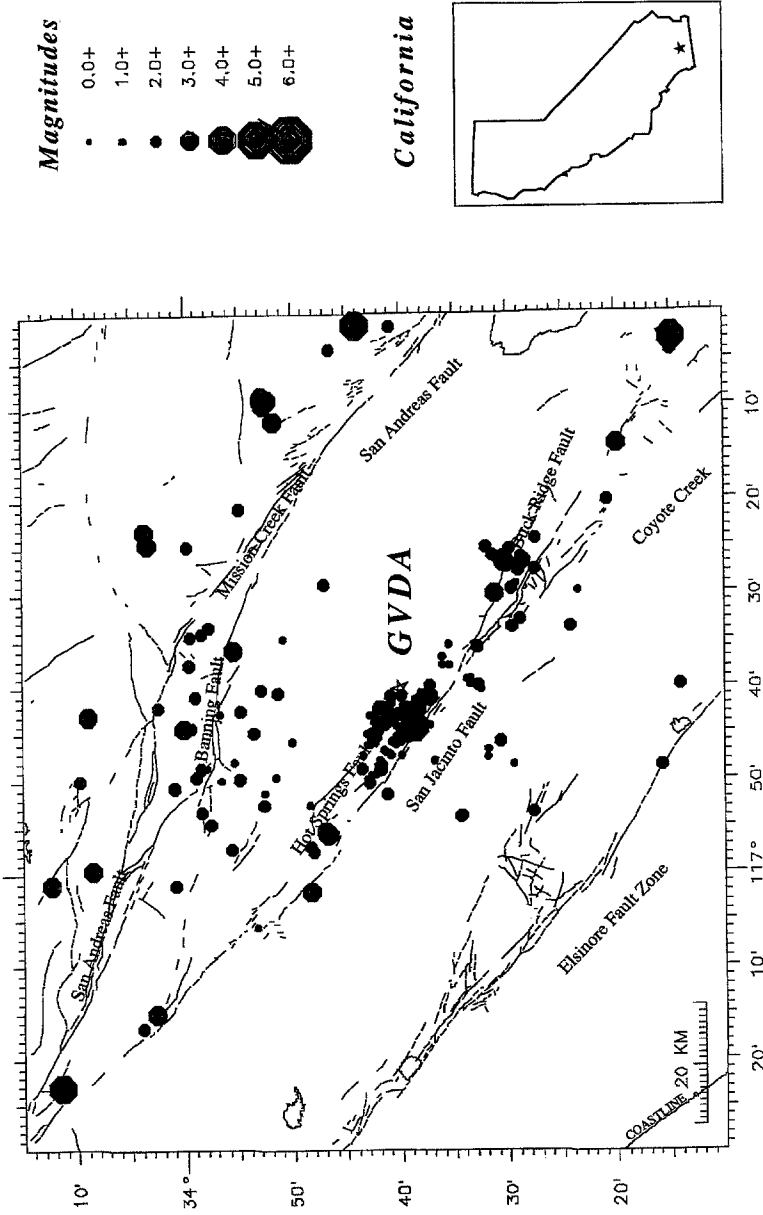


Fig. 6. Map view of the region around GVDA showing faults and the epicenters of the 280 earthquakes that have been recorded at GVDA from July 1989 to May 1991.

TABLE 2
EARTHQUAKE PARAMETERS

	Origin Time (y/m/d h.m.s)	Magnitude*	Latitude (°N)	Longitude (°W)	Epicentral Distance (km)	Depth (km)	Hypocentral Distance* (km)	(° clockwise from N)	Figure Event is Used in
1	89/07/22 07.35.11	2.7	33 39.84	116 45.03	6.6	14.11	15.6	266.46	9, 10
2	89/08/30 18.39.08	3.1	33 55.55	116 36.22	29.2	12.50	31.7	15.09	9
3	89/09/09 11.25.52	2.2	33 39.30	116 43.66	5.4	15.04	16.0	255.84	9, 10
4	89/11/11 06.49.27	1.9	33 37.38	116 44.28	8.2	1.11	8.3	234.85	9
5	89/11/19 00.03.42	2.0	33 39.68	116 45.40	7.6	13.80	15.8	264.90	7, 10
6	89/11/21 05.44.07	2.0	33 40.08	116 45.82	8.2	13.88	16.1	269.49	9, 10
7	89/12/02 23.12.04	2.3	33 38.90	116 44.63	7.0	14.36	16.0	253.90	10
8	89/12/02 23.16.47	4.2	33 38.74	116 44.50	6.2	14.47	15.8	251.40	7, 8, 9, 10, 11, 13
9	89/12/06 19.15.23	3.4	33 48.42	117 2.13	36.8	15.33	39.9	290.87	9
10	89/12/08 06.10.09	2.5	33 38.68	116 44.15	6.6	13.32	14.9	249.00	8, 9, 10, 12, 13
11	89/12/11 14.57.06	2.5	33 39.98	116 41.11	0.0	15.35	15.4	258.58	9, 10
12	89/12/18 06.27.04	4.0	33 44.03	116 1.43	60.4	9.93	61.2	84.28	9
13	89/12/21 04.47.13	2.0	33 42.01	116 42.25	3.8	17.43	17.8	315.13	9
14	89/12/22 03.03.25	3.4	33 37.44	116 41.27	5.4	14.08	15.1	198.38	7, 9, 10
15	89/12/28 09.41.08	4.3	34 11.54	117 23.18	87.8	14.58	89.0	306.27	9
16	89/12/30 10.16.14	2.8	33 30.18	116 27.34	27.3	9.03	28.7	127.35	9
17	90/01/07 23.13.57	2.1	33 42.16	116 44.32	7.0	17.18	18.5	297.26	10
18	90/01/10 12.33.06	2.3	33 53.70	116 45.03	26.0	16.49	30.8	341.08	9
19	90/03/01 03.23.03	4.7	34 9.15	117 43.21	110.6	11.43	111.2	294.79	7, 9
20	90/03/02 17.26.25	4.6	34 8.70	117 41.68	108.1	5.61	108.3	294.99	9
21	90/04/13 17.29.07	2.2	33 32.83	116 40.01	13.6	11.83	18.0	177.12	10
22	90/04/16 23.58.21	2.0	33 43.66	116 48.97	14.8	19.18	24.2	292.34	10
23	90/05/10 07.23.36	2.1	33 39.62	116 43.28	3.8	15.31	15.8	260.07	10
24	90/05/14 05.05.27	2.6	33 32.89	116 35.97	14.9	14.11	20.5	148.66	10
25	90/06/11 21.18.34	2.2	33 41.86	116 48.57	12.8	16.53	20.9	281.94	10
26	90/06/19 01.55.22	2.4	33 41.29	116 51.66	17.5	13.27	21.9	275.88	10
27	90/06/26 11.53.16	2.0	33 38.18	116 42.72	4.9	17.05	17.7	230.26	10

The horizontal accelerations recorded at 220 m and at the surface for four earthquakes are shown in Figures 7a and b, respectively. In each figure the accelerograms are arranged from top to bottom in ascending order of their magnitudes: 2.0, 3.4, 4.2, and 4.7 (events 5, 14, 8, and 19, respectively, Table 2). The M 2.0, 3.4, and 4.2 earthquakes are all at the same hypocentral distance of 16.2 km (within ± 0.5 km) from GVDA. The M 4.7 earthquake, one of the Upland aftershocks discussed above, is 110 km from GVDA and has the smallest amplitude of the four earthquakes shown. A comparison of Figures 7a and b shows the similarity in the waveforms and the amplification of the surface traces compared to the time histories at 220 m. The surface peak accelerations are amplified by factors ranging from 3 to 6 with the smaller amplitudes at 220 m being amplified more than the larger amplitudes.

To better understand the amplification, we examined in detail the Fourier displacement amplitude spectrum of 17 earthquakes that ranged in magnitude from 1.5 to 4.7. The displacement spectrum of S waves can be used to determine the earthquake source parameters—seismic moment, corner frequency, and source spectral decay—plus attenuation due to the propagation of the seismic waves (Brune, 1970, 1971; Boatwright, 1978). The source spectral decay (often referred to as spectral fall-off γ) and the intrinsic attenuation κ_0 due to propagation are difficult to separate. There is a lot of seismic evidence that the displacement spectrum amplitude decays as f^{-2} , $\gamma = 2$ (e.g., Aki, 1968; Brune, 1970; Hanks, 1979). Thus if one assumes $\gamma = 2$, the intrinsic attenuation can be determined from the spectrum.

The low-frequency asymptote (LFA or Ω_0) is directly proportional to the seismic moment of the earthquake. Assuming that the earthquakes all have similar focal mechanisms, the LFA for different earthquakes can be compared if they are normalized by the hypocentral distance assuming $1/R$ geometrical spreading. We have used the Simplex algorithm to determine the best fit to the seismic spectrum given free parameters of Ω_0 , corner frequency, and κ_0 , ignoring attenuation in the deeper granite (Lindley and Archuleta, 1989, 1992). The source spectral fall-off γ is fixed at 2.0, and we have assumed that Q is frequency independent. Examples of this procedure are shown in Figure 8 where we have determined the best fit to the S -wave displacement spectrum at 0 and 220 m for the M_L 4.2 and 2.5 earthquakes (events 8 and 10, Table 2). Almost all of the 17 earthquakes we studied have corner frequencies above 5.0 Hz and in many cases greater than 10 Hz. By taking a fixed window length for the Fourier analysis of the strongest S waves, we have limited our analysis to frequencies above 0.5 Hz. Thus in our analysis Ω_0 is a good measure of the spectral level for frequencies between ≈ 1 to 10 Hz and gives an apparent seismic moment. The true seismic moment could be determined only if Ω_0 were determined from much lower frequencies. For each earthquake, we computed the spectral fit to S waves as recorded on the two horizontal components. Although resonances exist, as discussed below, the spectral fitting routine is not very sensitive to narrow peaks in the spectra (Fig. 8). After scaling by hypocentral distance R we plotted the scaled Ω_0 at the surface versus the value at 220 m (Fig. 9). A linear least-squares fit to the data yields the relationship

$$\log(\Omega_0[0] \times R) = 1.1 + 0.82 \log(\Omega_0[220] \times R) \quad (3)$$

with a correlation coefficient r^2 of 0.95. For five orders of magnitude in the size

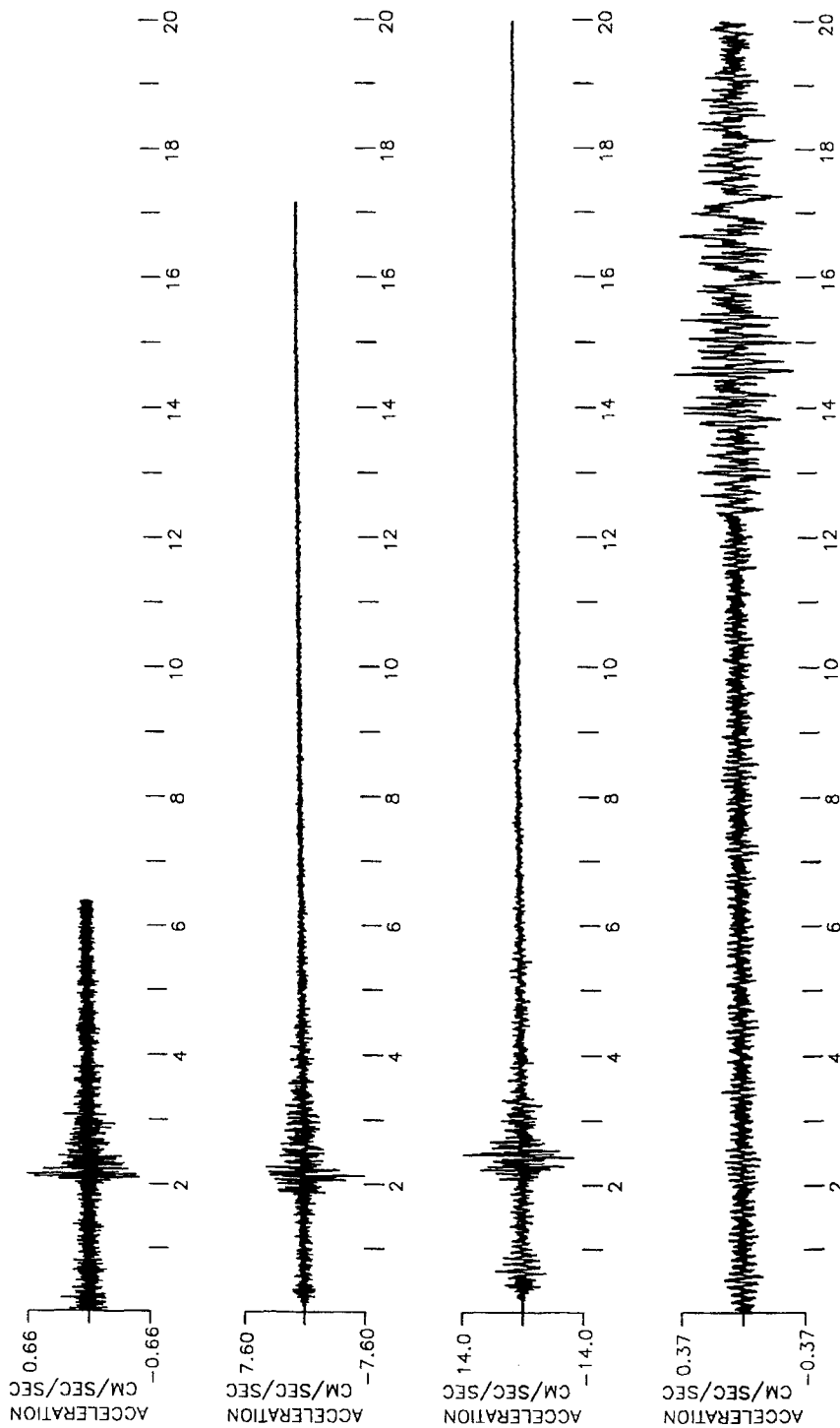
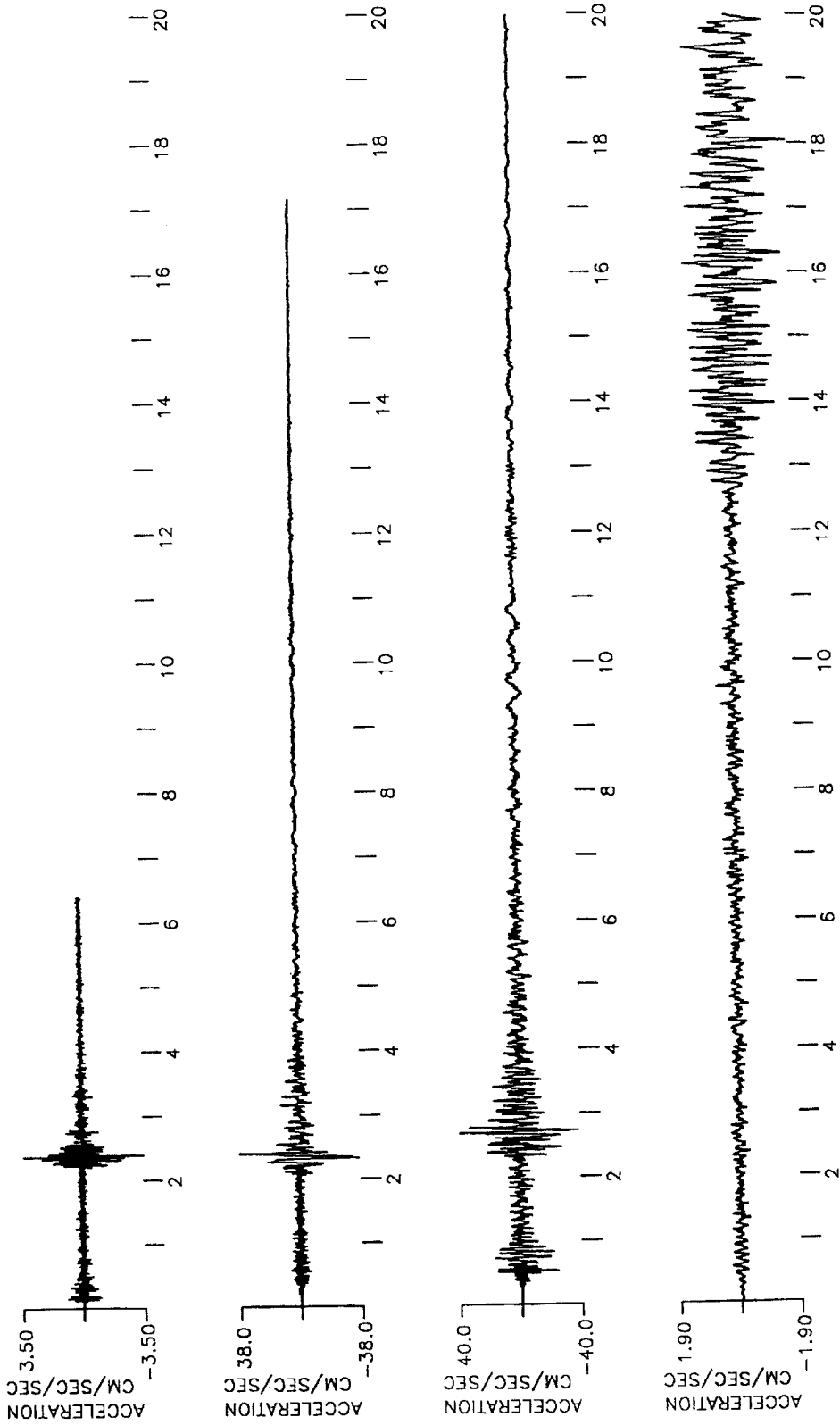


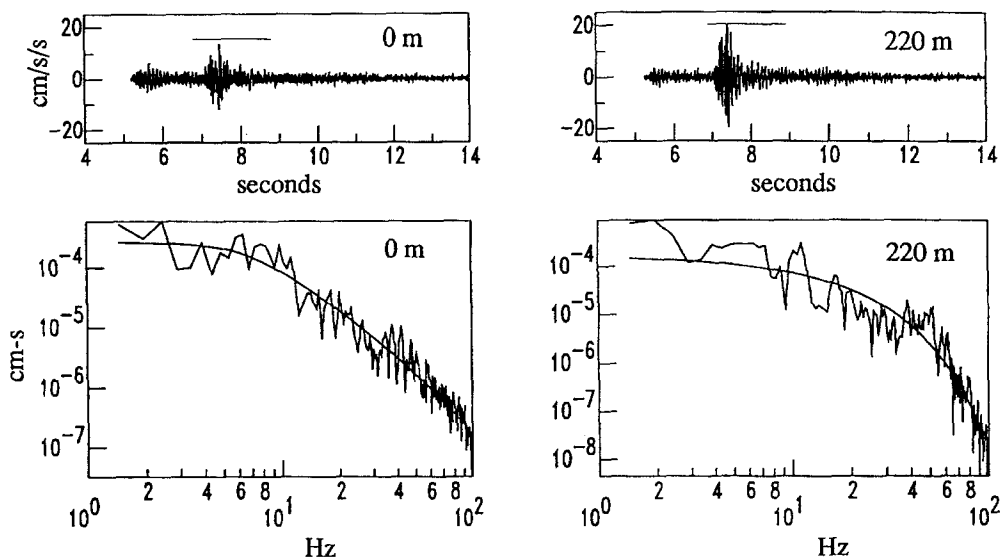
FIG. 7 (a) Horizontal components of acceleration at 220 m from four earthquakes. The events have M 2.0, 3.4, 4.2, and 4.7 and are arranged from top to bottom. The M 4.7 earthquake is 110 km from GVDA; the others are all at 16.2 ± 0.5 km (hypocentral distance). (b) Surface records for the events shown in Figure 7a.



SECONDS

FIG. 7 (b).

Magnitude 4.2



Magnitude 2.5

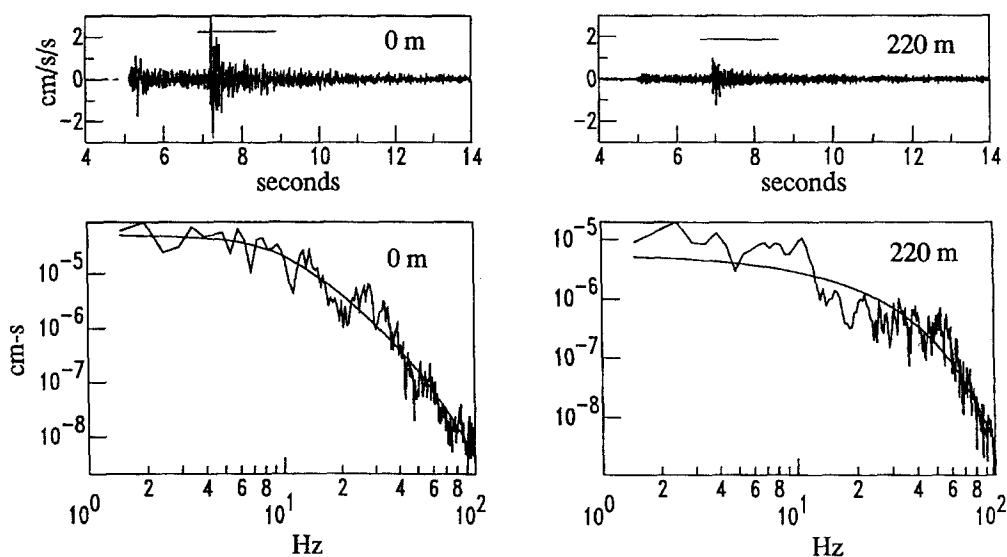


FIG. 8. Fourier displacement amplitude spectra of four of the horizontal accelerations recorded at the surface and at 220 m depth from events 8 and 10 (Table 2), M 4.2 and 2.5, respectively. The smooth line is a nonlinear fit to the data. The low-frequency asymptote is proportional to the apparent seismic moment as discussed in the text.

of the earthquakes, there is almost a linear relationship between the amplification of records at the surface and those recorded downhole.

The intercept value of 1.1 can be interpreted as the low-frequency amplification: for a unit amplitude of ground motion at 220 m, the ground motion will be $10^{1.1}$ or 12.6 times larger at the surface. The amplification factor that includes the impedance contrast and the free-surface effect is calculated as 7.2 for waves

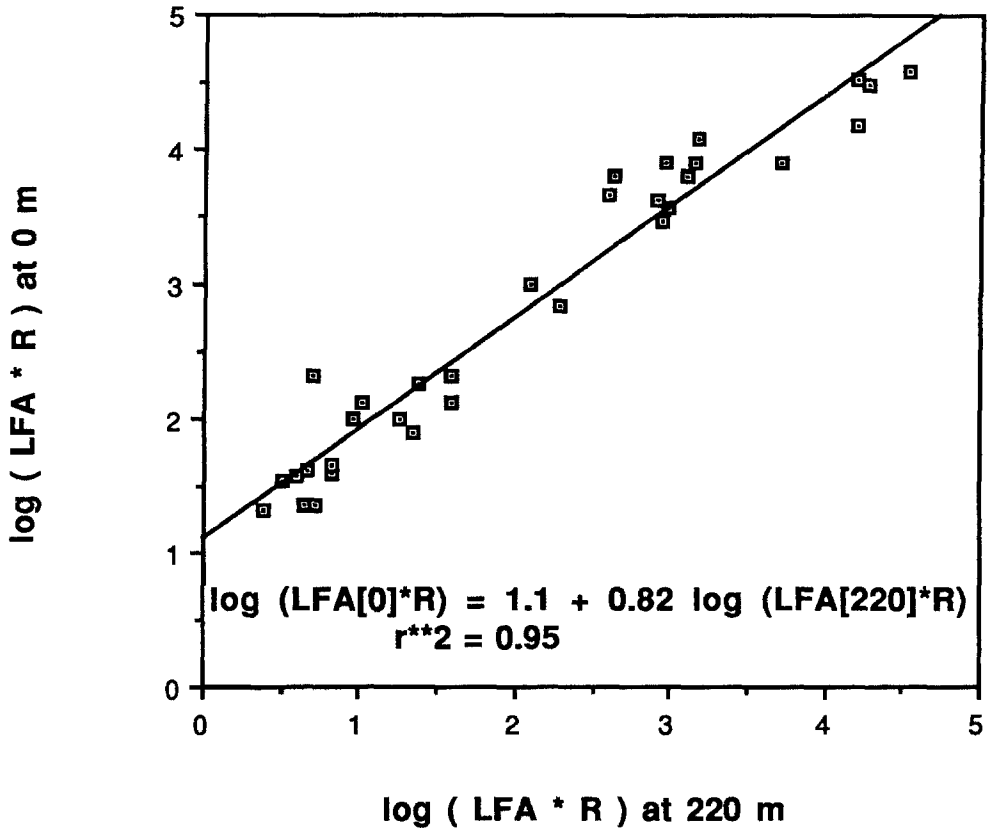


FIG. 9. Low-frequency asymptote (LFA) at 0 m plotted versus LFA at 220 m. Both LFA are scaled by hypocentral distance R . The LFA is computed for both horizontal components of 17 earthquakes studied. LFA is directly proportional to the size of the earthquake. Over five orders of magnitude in earthquake size, the amplitude at the surface is linearly related to the amplitude at depth.

with vertical incidence and no resonance, assuming a material density of 2.8 gm/cm^3 and S -wave velocity of 2800 m/sec for the granite and 2.4 gm/cm^3 and 220 m/sec for the soil. The slope of the regression line being less than 1.0 suggests that the larger earthquakes are amplified less than the smaller ones. However, this does not say anything about linear versus nonlinear effects because the largest earthquake M_L 4.7 had the smallest amplitude (Figs. 7a and b).

This analysis has an implicit wavelength dependence that was discussed earlier. The amplitude of waves with wavelengths much greater than the depth of the layer of near-surface material will not be affected by the layer (Shearer and Orcutt, 1987). At zero frequency there is no amplification, but for frequencies whose quarter wavelength is less than the layer depth there is amplification. Thus the impedance amplification has a frequency dependence that could result in the slope being less than one. The larger earthquakes have lower corner frequencies. As the corner frequency decreases, the wavelength increases and the amplification decreases. Likewise we must view the amplification factor of 12.6 as being appropriate for a limited frequency range.

To examine more closely the amplification as a function of frequency, we selected 17 earthquakes with $M \geq 2.0$ that were within 20 km of GVDA (Table

2). For each of the 17 earthquakes we computed a whole record spectral ratio of surface to 220 m for each of the horizontal components. The earthquakes occur at many different azimuths with respect to GVDA; we have computed the average spectral ratio from the 17 earthquakes (Fig. 10). The upper plot (Fig. 10) shows the average spectral ratios 0/220 and 22/220 for one of the horizontal components; the lower plot shows the average spectral ratios 0/220 and 22/220 for the other horizontal component. In both plots the greater spectral ratio is the 0/220. We have not smoothed any of the records; some of the very spiky peaks are likely to be due to holes in the spectrum at 220 m rather than a resonance in the soil. The spectral ratios of each component are quite similar. Ignoring the peaks, the average level of amplification is around 10 in the frequency band 1.5 to 30 Hz. This amplification is very close to that determined from examining the displacement spectra (Fig. 9). The resonances around 1.7, 3.0, and 12 Hz are evident for both components. There is a low-frequency resonance around 0.4 Hz that shows up on only one component. Both plots show that the spectral ratio is rapidly decreasing above 35 Hz.

The effect of the weathered granite layer can be examined by examining the spectral ratios 22/220 (Fig. 10). The average level of the spectral ratio between 2.0 and 30 Hz is around three. One of the more obvious features is the large resonance around 1.7 Hz on the lower plot. The overall shape of the spectral ratio observed for 22/220 is very similar to that for 0/220, which is simply a factor of 3 or so larger. Thus the weathered granite layer amplifies the waves before they reach the soil. We observed a similar situation for other downhole strong motion records at McGee Creek, California, where an intermediate layer strongly affected the overall amplification of seismic waves (Seale and Archuleta, 1989).

In order to examine the effect of the different layers, we examine the acceleration amplitude spectra of *S* and *P* waves at each depth for two earthquakes that occurred close to each other. In this way, we can minimize effects due to path, distance, or azimuth and compare records that have very different amplitudes. In Figures 11 and 12, we show the acceleration amplitude spectra for each depth for the *M* 4.2 (event 8, Table 2) earthquake and the *M* 2.5 (event 10, Table 2) earthquake, respectively. The *S*-wave spectral amplitudes are the root-mean-square (RMS) of the two horizontal spectra. The *P*-wave acceleration amplitude spectra are the Fourier transform of the *P* waves on the vertical component at each depth. The Fourier transforms were computed over a 2-sec time window and all spectra have been smoothed over a 3-Hz band.

These data reveal several features. For *S* waves, the spectrum at 220 m has a significantly greater amount of high-frequency energy than at any other depth (Figs. 11 and 12). If the amplitude at low frequencies for 0 m is adjusted to be comparable to the low-frequency amplitude at 22 m by multiplying by about 2.2, the high-frequency spectral amplitudes at 0 m exceed the spectral amplitudes at 22 m by a factor of 20 or so for both events at frequencies greater than 40 Hz. The sensor at 22 m is located in the weathered granite zone just below the soil. We infer that, while the weathered granite zone has amplified the low frequencies, the attenuation exceeds the amplification at high frequencies. The overall spectrum of the record at 22 m is again amplified by the soil, as can be seen by comparing its spectrum with that at the surface (Figs. 11 and 12). A curious feature is that the spectral amplitudes at 0, 6, and 15 m exceed the spectral

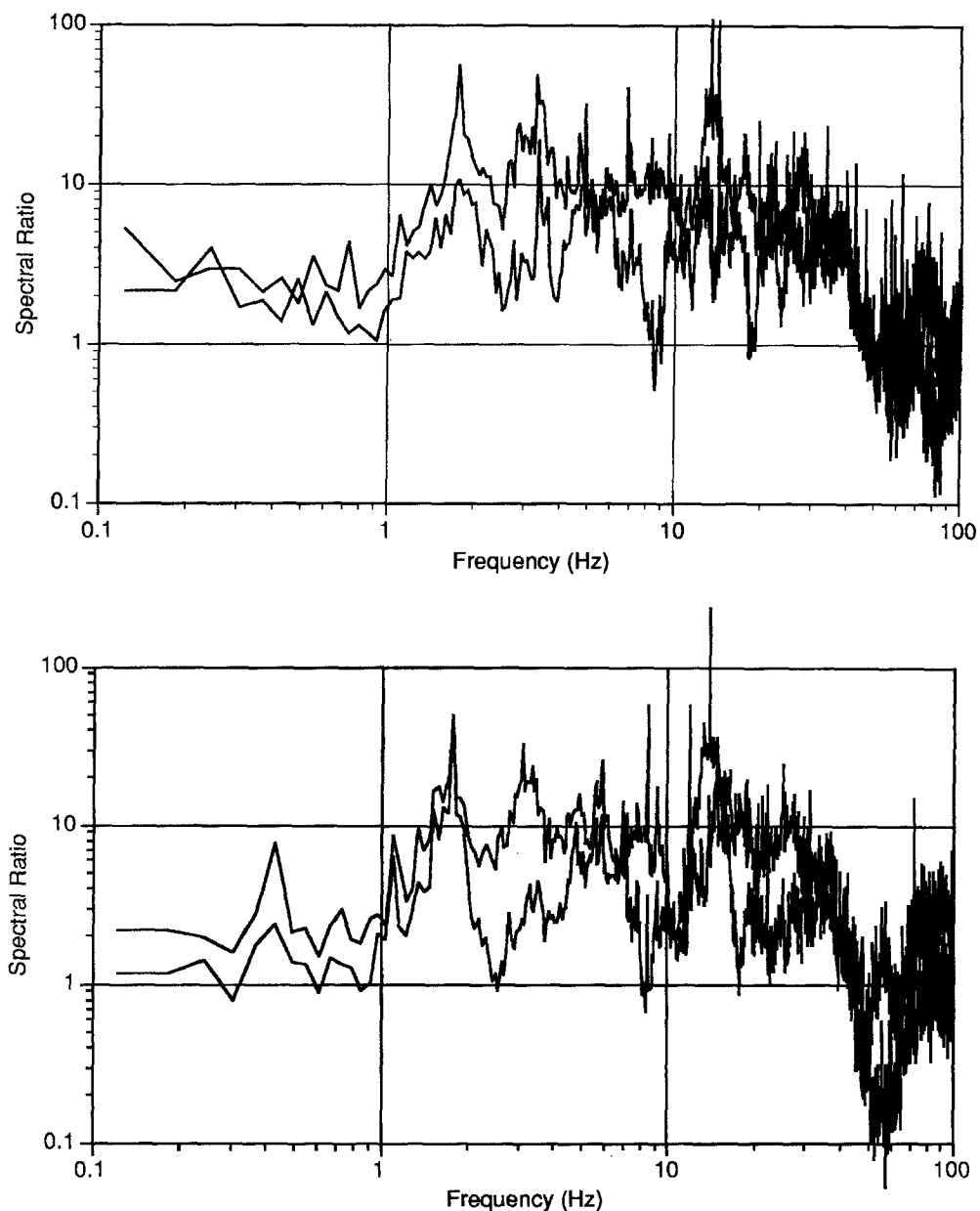


FIG. 10. Average of 17 spectral ratios from accelerograms at 0 and 220 m plotted with the average of 10 spectral ratios from accelerograms at 22 and 220 m. The two plots are spectral ratios for the two horizontal components. For each horizontal component of every earthquake, the acceleration amplitude spectrum at the surface and at 22 m was divided by the amplitude spectrum at 220-m depth. The spectral ratios were then averaged. The mean amplification at the surface is around 10 for 2 to 30 Hz, but the resonances are as high as 40 to 50 and are observed in both components. The spectral ratios for the 22-m depth are dominated by the properties of the weathered granite layer (Fig. 2) and have a mean level that is about a factor of 3 lower than those at the surface. The very large spikes are due to holes in the spectra at 220 m. Attenuation becomes evident around 35 Hz.

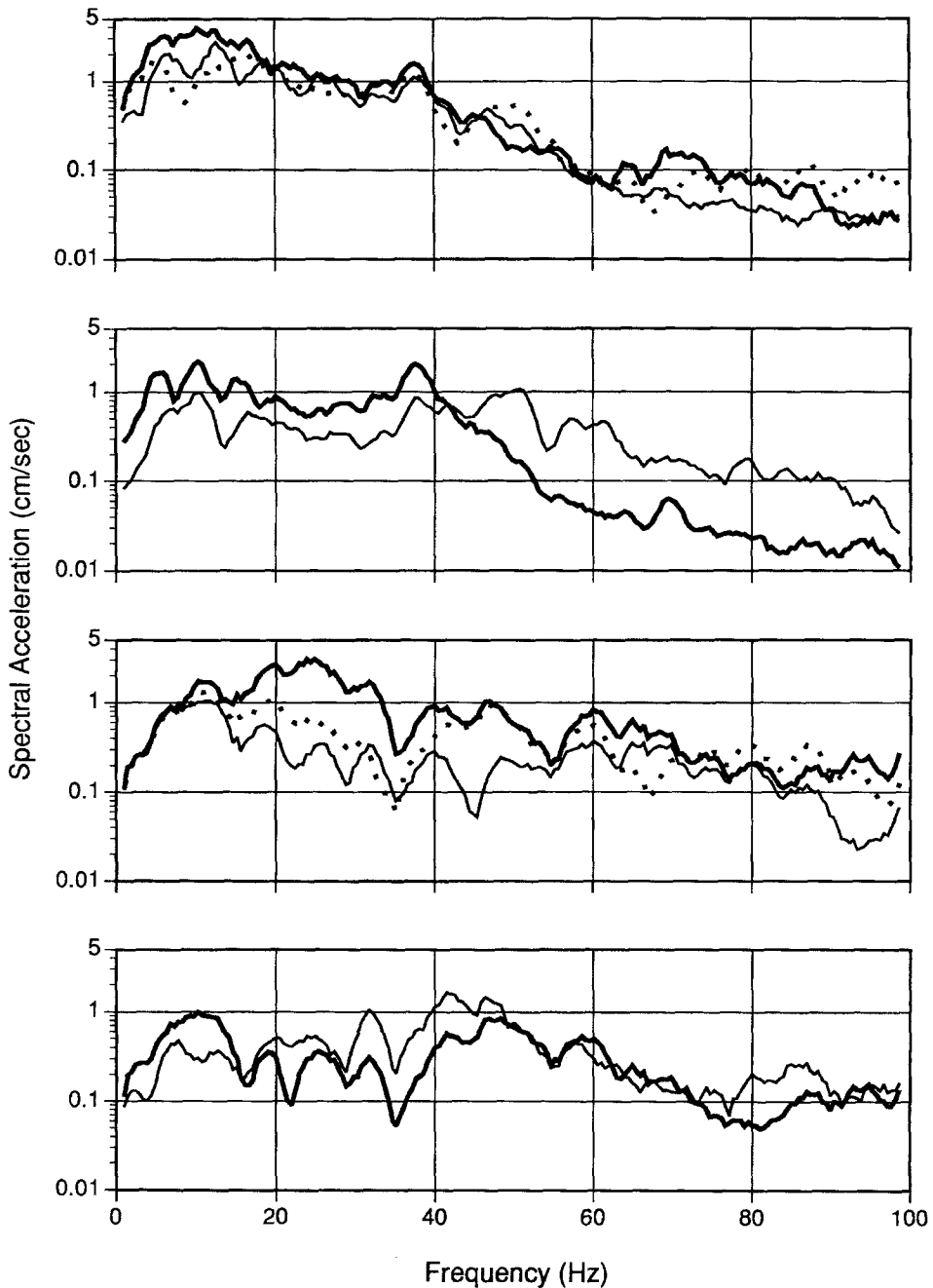


FIG. 11. Acceleration amplitude *S*-wave and *P*-wave spectra for each downhole accelerometer for an M_L 4.2 earthquake, event 8. The *S*-wave spectra are the root-mean-square amplitudes of the two horizontal *S*-wave spectra. The *P*-wave spectra are the amplitudes of the Fourier transform of the *P* waves on the vertical component. The Fourier transforms have been computed over a 2-sec time window, and all spectra have been smoothed by taking a running mean over a 3.0-Hz frequency band. In the plots showing three spectra, the dark solid line, light solid line, and dashed line correspond to 0-, 6-, and 15-m depths, respectively. In the plots showing two spectra, the dark solid line and light solid line correspond to 22- and 220-m depths respectively.

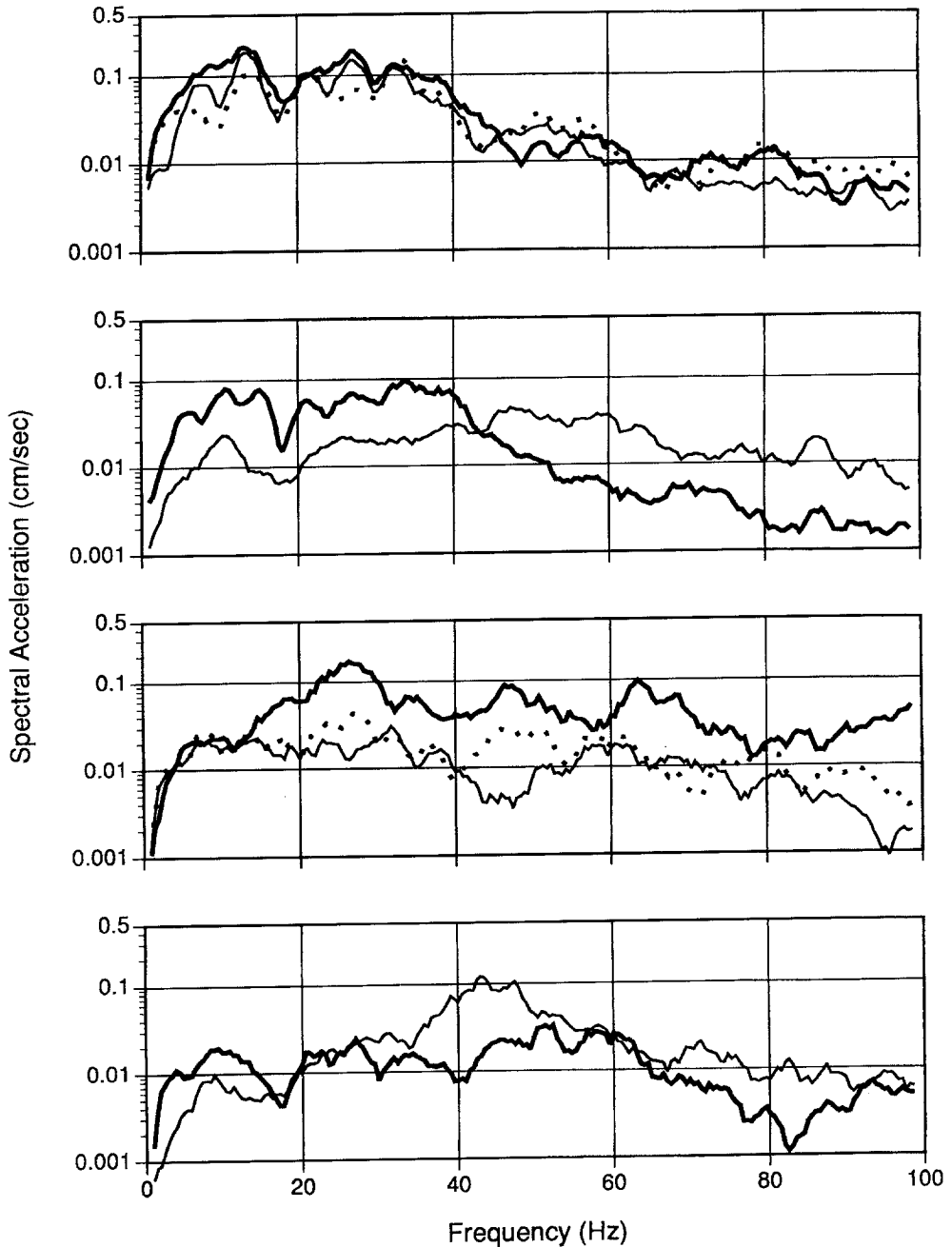


FIG. 12. Acceleration amplitude *S*-wave and *P*-wave spectra for each downhole accelerometer for an M_L 2.5 earthquake, event 10. See caption of Figure 11 for details.

amplitudes at 22 m in the range from 60 to 100 Hz. This would imply that the amplification factor exceeds the attenuation in the soil in this frequency range. This result needs more study to understand how the *P*-wave coda, which is part of the time series for the *S* wave, might be affecting this preliminary interpretation.

There are definite peaks and troughs that are correlated from depth to depth (Figs. 11 and 12). The amplitude of these peaks relative to each other for one depth changes from depth to depth. For example, the largest spectral peak at 6 m is around 40 Hz, while the largest spectral peak at 15 m is about 13 Hz. Nonetheless both peaks clearly exist at both depths. By comparing the spectra from these two events, it is obvious that the same spectral peaks exist for both earthquakes, although the strength of the peaks is different between the two spectra.

The *P*-wave spectra have a much different shape compared to the *S*-wave spectra (Figs. 11 and 12). In general, the *P*-wave spectra show less attenuation than the *S*-wave spectra. At 220 m, the *P*-wave spectrum has almost the same amplitude as the *S*-wave spectrum for frequencies greater than 20 Hz. At the surface, the *P*-wave spectrum generally equals or exceeds the *S*-wave spectrum for frequencies greater than 20 Hz. At all depths, the *P*-wave spectral amplitudes are equal to or greater than the *S*-wave amplitudes for frequencies greater than 50 Hz. One exception is the 15-m depth for the M_L 2.5 earthquake (Fig. 12). Certainly the most dramatic example is the comparison of the *P*- and *S*-wave spectra at 0 m with those at 220 m for the M_L 4.2 earthquake (Fig. 11). At 220 m, the *P*- and *S*-wave spectra are nearly the same (within a factor of 2 or 3) for frequencies greater than 20 Hz; yet, at the surface, the *P*-wave spectrum is significantly larger for all frequencies greater than 20 Hz. On average, the attenuation of the *P* waves is much less than that of the *S* waves.

To compare the relative differences between 220 m and other depths, we computed the spectral ratios for all depths relative to the spectrum at 220 m. The spectral ratios 0/220 and 22/220 for the two events M_L 4.2 and M_L 2.5 are shown in Figure 13. Because the spectra at 6 and 15 m are so similar to those at the surface (Figs. 11 and 12), we do not show these ratios. The similarity of the *S*-wave spectral ratios for the two events stands out. The M_L 2.5 spectral ratio 0/220 is greater than that of the M_L 4.2 event. There is a very strong similarity between the spectral ratio 0/220 and 22/220. As noted previously, the amplification factor of 2 to 2.5 between the ratios 0/220 and 22/220, out to about 35 Hz, is caused by the soil column. The large peak around 17 Hz is due to a hole in the spectrum at 220 m (Figs. 11 and 12) and not due to resonance. While one might have expected the *S*-wave spectral ratio for both 0/220 and 22/220 to consistently decrease due to attenuation, that does not occur. The spectral ratios show an increase or leveling off starting around 50 Hz. The overall spectral *S*-wave amplification at low frequencies is around 9, which is similar to what we determined by averaging the spectra of 17 earthquakes (Fig. 10).

Inspection of *P*-wave spectral ratios (Fig. 13) shows strong amplification in this 60- to 100-Hz frequency range. This implies that the *P*-wave coda can exceed the *S*-wave coda in this frequency range, thereby giving the observed spectral ratio for *S* waves above 10 Hz. That is, the windowed *S*-wave spectrum is a combination of both the actual *S*-wave spectrum and the *P*-wave spectrum. Above 60 Hz, the *P*-wave spectrum dominates because of the amplification in the soil and weathered granite. The other major feature is the strong amplification at the surface seen in the 0/220 ratio for both the M_L 4.2 and 2.5 earthquakes. Comparing the 0/220 ratio to the 22/220 ratio, it is clear that the soil column has strongly amplified the vertical component of motion.

Lastly, there is the scaling of the overall shape of the acceleration spectra for the two earthquakes. The two earthquake spectra scale as if each had the same

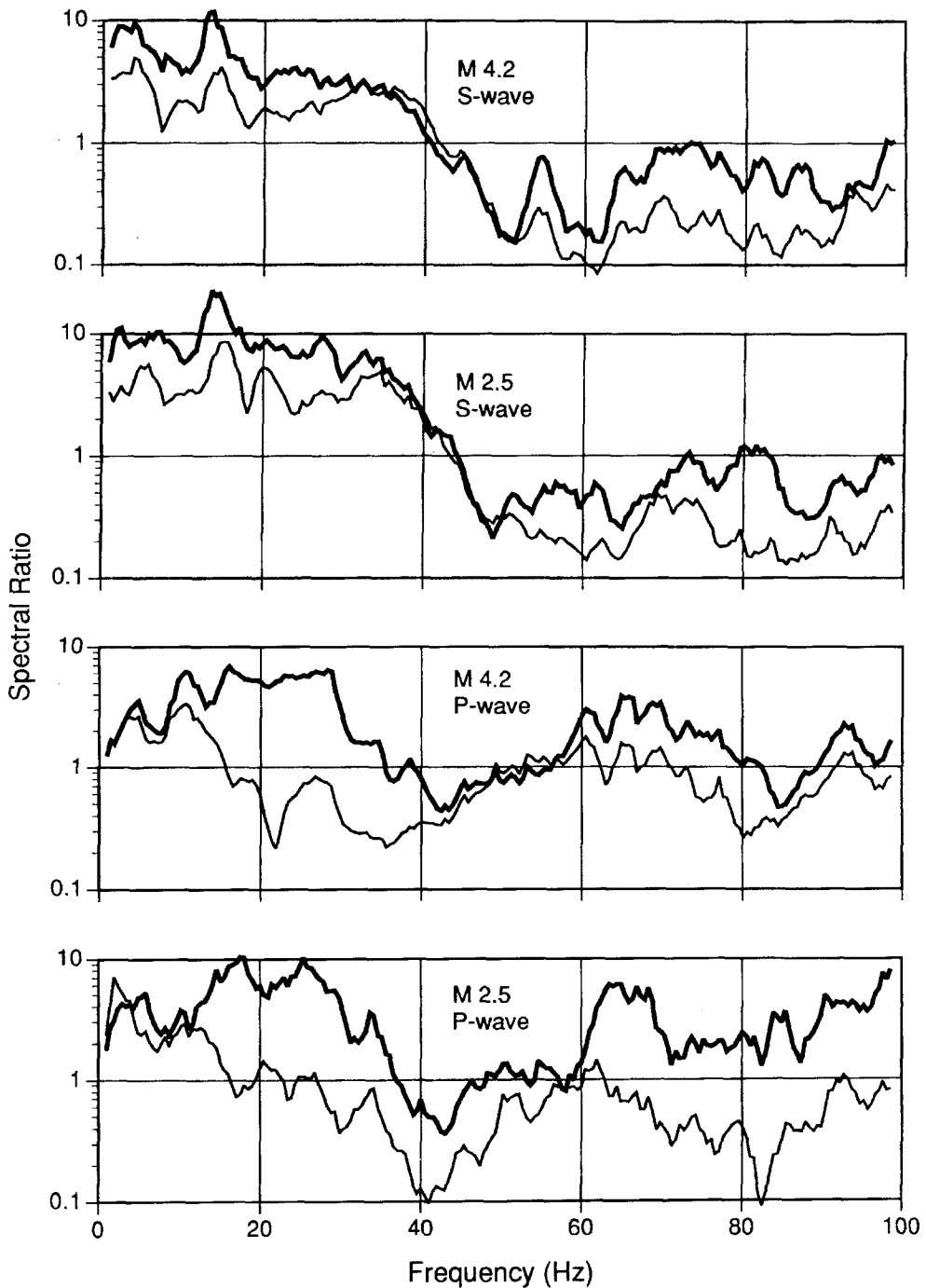


FIG. 13. *S*-wave and *P*-wave spectral ratios 0/220 and 22/220 for the M_L 4.2 and 2.5 earthquakes, events 8 and 10. In each plot the dark line and light line correspond to the 0/220 and 22/220 ratios, respectively. Note the strong attenuation of the *S*-wave ratios for frequencies greater than 35 to 40 Hz. The average *S*-wave spectral ratio at frequencies less than 20 Hz is around 8 to 12. The *P*-wave spectral ratios show a pronounced amplification for frequencies less than 20 Hz and again around 50 to 90 Hz.

stress drop in that the spectra can be equalized in the low frequencies ($f < 10$ Hz) by multiplying the spectra of event 10, M_L 2.5, by 35 and the spectral amplitudes of the high frequencies by the cube root of 35 (Joyner and Boore, 1986). The multiplicative factor, 35, is consistent with the relationship $\log M_0 = 1.1 M_L + 17$, which is approximately that found for other small magnitude earthquakes (Archuleta *et al.*, 1982; Bakun, 1984; Vidal and Munguia, 1991), assuming that the magnitude given by the USGS is equivalent to M_L .

Admittedly, acceleration spectra on a log-linear plot are not ideal for examining source parameters such as moment and corner frequency. However, such plots are useful for examining the effects of attenuation (Anderson and Hough, 1984). Although there is significant variation, the *S*-wave spectral level at 220 m is basically flat for frequencies between 10 and 60 Hz (Figs. 11 and 12). Beyond 60 Hz the spectral level shows a definite decrease, from which one might compute a quality factor for the granitic batholith that underlies Garner Valley. The question is whether to smoothly draw a line through the large spectral amplitudes between 30 and 60 Hz. Until we understand the origin of the spectral amplitudes in this range, there is a lot of uncertainty in the determination of Q .

The problem of determining Q becomes more difficult for the shallower depths. The spectra are dominated by the dramatic decrease in the amplitudes that starts around 40 Hz (Figs. 11 and 12). This decrease occurs between 220 and 22 m. The soil impedance boosts the spectral amplitudes such that the spectral level at 0 m is greater in the high frequencies than it is at 22 m. The spectral ratios (Fig. 13) show that the spectral levels at the shallower depths are slowly decreasing as frequency increases, if at all, until around 40 Hz, at which point the spectral ratio drops immediately. This decrease is due to the attenuation in the weathered granite zone. In a depth of 200 m, the spectral amplitude has decreased by a factor of 30. A rough calculation yields a κ_0 of 0.027 corresponding to a Q of 12. These values will have to be examined more carefully using synthetic seismograms (Seale and Archuleta, 1989). Using only the surface record, the two earthquakes would give very different values of Q . The M_L 4.2 event has what appears to be a generally constant slope between 15 and 60 Hz; whereas the M_L 2.5 event has a relatively uniform level until 40 Hz, at which time the spectral amplitude decreases immediately. A final evaluation for Q will come after a more thorough analysis of all of the data.

SUMMARY

The Garner Valley downhole array of accelerometers is one of the few seismic stations that is directly measuring the effects of local site conditions on the amplification and attenuation of seismic waves. The vertical array of dual-gain accelerometers is capable of measuring accelerations from 3×10^{-6} to 2.0 *g* over a frequency range from 0.0 (0.025, high-gain) to 100 Hz. Since installation in July 1989, GVDA has recorded 280 earthquakes with magnitudes from 1.1 to 4.7. The maximum acceleration recorded was 89 cm/sec² on the vertical component at the surface. By analysis of the Fourier amplitude spectrum for various earthquakes, the average amplification due to the local geology and to the free surface is about 13 for over five orders of magnitude in the size of the earthquakes. The average spectral ratio of horizontal acceleration amplitude spectrum at the surface divided by the amplitude spectrum at 220 m shows a mean amplification around 10. Definite resonance peaks exist at about 1.7, 3.0,

and 12.0 Hz, where the spectral ratio is nearly 40. Analysis of spectral ratios for depths 22 to 220 m shows an overall mean level that is about a factor of 3 lower than the 0 to 220 m ratio. However, the spectral ratio for 22/220 shows similar resonance peaks. Both average spectral ratios 0/220 and 22/220 show large attenuation of the spectral amplitudes above 35 to 40 Hz.

Comparison of acceleration spectra from two earthquakes, M_L 4.2 and 2.5, which have nearly the same hypocentral location, shows that the near-surface amplification and attenuation is very similar for the two earthquakes. Their spectral ratios show the same behavior as the average amplitude spectra computed for several earthquakes (Fig. 10). Analysis of individual spectra and spectral ratios for the various depths shows that the zone of weathered granite has a pronounced effect on the spectral amplitudes for frequencies greater than 40 Hz. The soil layer impedance may amplify the high frequencies more than it attenuates them. This result must be checked more thoroughly with special consideration of the spectra of the P -wave coda in the horizontal accelerograms. Analysis of the P -wave spectra and the spectral ratios shows an increased amplification in the same frequency range (60 to 90 Hz) where the S -wave spectral ratios imply a change in the attenuation.

The analysis presented here is admittedly preliminary in that only a few of the 280 recorded earthquakes have been analyzed in detail. The purpose of this analysis has been to illustrate both the quality of the GVDA data and the complications created by site effects. It seems clear that deconvolving the site effect from a surface recording is not always straightforward. This is particularly true for the ground motion in the S -wave time window; that window includes not only the site effects for S waves but also the site effects on the P -wave coda. With the additional downhole accelerometer at 45 m and the complementary surface array, the Garner Valley arrays offer a unique opportunity to understand just how the local geology affects the seismic ground motion.

ACKNOWLEDGMENTS

Many individuals have assisted in the stages of planning, design, and drilling. We have welcomed the advice of Joe Fletcher, Tom Moses, and Jim Gibbs of the USGS. Richard Ledbetter of the Army Corps of Engineers was instrumental in the selection of the GVDA site. Jim Mori, Lucy Jones, and Tom Heaton of the USGS Southern California Network have cheerfully assisted us in acquiring the earthquake locations and magnitudes. Grant Lindley and Jamison Steidl at UCSB and Isabelle Sherjal at L.G.I.T., Université Joseph Fourier, Grenoble, have aided us in the spectral analysis of the data. We thank Michel Bouchon, L.G.I.T., Université Joseph Fourier, Grenoble, for many provocative and thoughtful discussions about the interpretation of the data. This paper was improved following comments of Paul Spudich, C. B. Crouse, and an anonymous reviewer. We are completely indebted to the Lake Hemet Municipal Water District (LHMWD) for allowing us to use its land for this experiment. In particular, we are grateful to Leonard Hale, general manager of LHMWD, for all of his support on our behalf. This research is supported by the Office of the Nuclear Regulatory Research, U.S. Nuclear Regulatory Commission Grant No. NRC-04-88-146 in cooperation with the French Commissariat à l'Energie Atomique and by the Electrical Power Research Institute, contract RP3014-90.

REFERENCES

- Aki, K. (1968). Scaling law of seismic spectrum, *J. Geophys. Res.* **72**, 1217-1231.
- Aki, K. (1988). Local site effects on ground motion, Earthquake Engineering and Soil Dynamics II—Recent Advances in Ground Motion Evaluation, *Proc. of the A.S.C.E. Speciality Conference*, Park City, Utah, June 27-30, 103-155.
- Anderson, J. G., P. Bodin, J. N. Brune, S. K. Singh, R. Quaas, and M. Onate (1986). Strong ground motion from the Michoacan, Mexico, earthquake, *Science* **233**, 1043-1049.

- Anderson, J. G. and S. E. Hough (1984). A model for the shape of the Fourier amplitude spectrum of acceleration at high frequencies, *Bull. Seism. Soc. Am.* **74**, 1969–1993.
- Archuleta, R. J. (1986). Downhole recordings of seismic radiation, in *Earthquake Source Mechanics*, S. Das, J. Boatwright, and C. Scholz, (Editors), 319–329.
- Archuleta, R. J., E. Cranswick, C. Mueller, and P. Spudich (1982). Source parameters of the 1980 Mammoth Lakes, California, earthquake sequence, *J. Geophys. Res.* **87**, 4595–4607.
- Aster, R. C. and P. M. Shearer (1991a). High-frequency borehole seismograms recorded in the San Jacinto fault zone, southern California, Part 1: polarizations, *Bull. Seism. Soc. Am.* **81**, 1057–1080.
- Aster, R. C. and P. M. Shearer (1991b). High-frequency borehole seismograms recorded in the San Jacinto fault zone, southern California. Part 2: attenuation and site effects, *Bull. Seism. Soc. Am.* **81**, 1081–1100.
- Bakun, W. H. (1984). Seismic moments, local magnitudes, and coda duration magnitudes for earthquakes in central California, *Bull. Seism. Soc. Am.* **74**, 439–458.
- Beeston, H. E. and T. V. McEvilly (1977). Shear wave velocities from down-hole measurements, *Earthquake Eng. Struct. Dyn.* **5**, 181–190.
- Berger, J., L. M. Baker, J. N. Brune, J. Fletcher, T. C. Hanks, and F. L. Vernon (1984). The Anza array: a high-dynamic range, broadband, digitally radiotelemetered seismic array, *Bull. Seism. Soc. Am.* **74**, 1469–1481.
- Blakeslee, S. and P. Malin (1991). High-frequency site effects at two Parkfield downhole and surface stations, *Bull. Seism. Soc. Am.* **81**, 332–345.
- Boatwright, J. (1978). Detailed spectral analysis of two small New York state earthquakes, *Bull. Seism. Soc. Am.* **68**, 1117–1131.
- Boatwright, J., J. B. Fletcher, and T. E. Fumal (1991). A general inversion scheme for source, site and propagation characteristics using multiply recorded sets of moderate-sized earthquakes, *Bull. Seism. Soc. Am.*, **81**, 1754–1782.
- Brune, J. N. (1970). Tectonic stress and spectra of seismic shear waves from earthquakes, *J. Geophys. Res.* **75**, 4997–5009. (Correction, *J. Geophys. Res.* **76**, 5002, 1971).
- Bullen, K. E. (1963). *An Introduction to the Theory of Seismology*, 3rd ed., Cambridge University Press, Cambridge.
- Carter, J. A., F. K. Duennebier, and D. M. Hussong (1984). A comparison between a downhole seismometer and a seismometer on the ocean floor, *Bull. Seism. Soc. Am.* **74**, 763–772.
- Çelebi, M. (1987). Topographical and geological amplifications determined from strong-motion and aftershock records of the 3 March 1985 Chile earthquake, *Bull. Seism. Soc. Am.* **77**, 1147–1167.
- Çelebi, M., J. Prince, C. Dietel, M. Oñate, and G. Chávez (1987). The culprit in Mexico City—amplification of motions, *Earthquake Spectra* **3**, 315–328.
- Cramer, C. H. and C. R. Real (1990). Turkey Flat, USA: site effects test area. Weak-motion test: statistical analysis of submitted predictions and comparisons to observations, Technical Report No. 90-2, California Division of Mines and Geology, Sacramento, California.
- Console, R. and A. Rovelli (1981). Attenuation parameters for Friuli region from strong motion accelerogram spectra, *Bull. Seism. Soc. Am.* **71**, 1981–1991.
- Cranswick, E., R. Wetmiller, and J. Boatwright (1985). High-frequency observations and source parameters of microearthquakes recorded at hard-rock sites, *Bull. Seism. Soc. Am.* **75**, 1535–1567.
- Fletcher, J., L. Haar, T. C. Hanks, and L. Baker (1987). The digital array at Anza, California: processing and initial interpretation of source parameters, *J. Geophys. Res.* **92**, 369–382.
- Fletcher, J. B., T. Fumal, H-P Liu, and L. C. Haar (1990). Near-surface velocities and attenuation at two boreholes near Anza, California, from logging data, *Bull. Seism. Soc. Am.* **80**, 807–831.
- Frankel, A. and L. Wennerberg (1989). Microearthquake spectra from the Anza, California, seismic network: site response and source scaling, *Bull. Seism. Soc. Am.* **79**, 581–609.
- Gibbs, J. F. (1989). Near-surface P- and S-wave velocities from borehole measurements near Lake Hemet, California, *U.S. Geol. Surv. Open-File Rep.* 89-630.
- Hanks, T. C. (1979). b values and $\omega^{-\gamma}$ seismic source models: implications for tectonic stress variations along active crustal fault zones and the estimation of high-frequency strong ground motion, *J. Geophys. Res.* **84**, 2235–2242.
- Hauksson, E., T. L. Teng, and T. Henyey (1987). Results from a 1500 m deep three-level downhole seismometer array: site response, low Q values and f_{max} , *Bull. Seism. Soc. Am.* **77**, 1883–1904.
- Hill, R. I. (1981). Geology of Garner Valley and vicinity, in *Geology of the San Jacinto Mountains*,

- Annual Field Trip Guidebook No. 9*, A. R. Brown and R. W. Ruff, (Editors), South Coast Geological Society, Santa Ana, California, 90–99.
- Hough, S. E., and J. G. Anderson (1988). High-frequency spectra observed at Anza, California: implications for Q structure, *Bull. Seism. Soc. Am.* **78**, 692–707.
- Housner, G. W. (1990). Competing against time, Report to Governor George Deukmejian from the Governor's Board of Inquiry on the 1989 Loma Prieta Earthquake, State of California, Office of Planning and Research, Sacramento, California.
- Jarpe, S. P., C. H. Cramer, B. E. Tucker, and A. F. Shakal (1988). A comparison of observations of ground response to weak and strong motion at Coalinga, California, *Bull. Seism. Soc. Am.* **78**, 421–435.
- Johnson, L. R. and W. Silva (1981). The effects of unconsolidated sediments upon the ground motion during local earthquakes, *Bull. Seism. Soc. Am.* **71**, 127–142.
- Joyner, W. B. and D. M. Boore (1986). On simulating large earthquakes by Green's-function addition of smaller earthquakes, in *Earthquake Source Mechanics*, S. Das, J. Boatwright, and C. Scholz (Editors), 269–274.
- Joyner, W. B., R. E. Warrick, and A. A. Oliver, III (1976). Analysis of seismograms from a downhole array in sediments near San Francisco Bay, *Bull. Seism. Soc. Am.* **66**, 937–958.
- King, J. L. and B. E. Tucker (1984). Observed variations of earthquake motion across a sediment-filled valley, *Bull. Seism. Soc. Am.* **74**, 137–151.
- Lindley, G. T. and R. J. Archuleta (1989). Differences between sites in the variability of the Fourier spectra of earthquakes, *EoS* **70**, 1189.
- Lindley, G. T. and R. J. Archuleta (1992). Earthquake source parameters and the frequency dependence of attenuation at Coalinga, Mammoth Lakes and the Santa Cruz Mountains, California, *J. Geophys. Res.* (in press).
- Lindley, G. T., R. J. Archuleta, and G. Maxwell (1987). Least squares fit of earthquake spectra in the Mammoth Lakes area of California, *EoS* **68**, 1362.
- Liu, H.-S. and T. H. Heaton (1984). Array analysis of the ground velocities and accelerations from the 1971 San Fernando, California, earthquake, *Bull. Seism. Soc. Am.* **74**, 1951–1968.
- Liu, H.-P., R. E. Warrick, R. E. Westerlund, J. B. Fletcher, and G. L. Maxwell (1988). An air-powered impulsive shear-wave source with repeatable signals, *Bull. Seism. Soc. Am.* **78**, 355–369.
- Malin, P. E., J. A. Waller, R. D. Borchardt, E. Cranswick, E. G. Jensen and J. Van Schaack (1988). Vertical seismic profiling of Oroville microearthquakes: velocity spectra and particle motion as a function of depth, *Bull. Seism. Soc. Am.* **78**, 401–420.
- Mueller, C. S. (1986). The influence of site conditions on near-source high frequency ground motion: case studies from earthquakes in the Imperial Valley, Ca., Coalinga, Ca., and Miramichi, Canada, *Ph.D. Thesis*, Stanford University, Stanford, California.
- Pecker, A. and B. Mohammadioun (1991). Downhole instrumentation for the evaluation of nonlinear soil response on ground surface motion, 1991 SMIRT Conference, Tokyo.
- Rockwell, T., C. Loughman and P. Merifield (1990). Late Quaternary rate of slip along the San Jacinto fault zone near Anza, southern California, *J. Geophys. Res.* **95**, 8593–8605.
- Rogers, A. M., J. C. Tinsley, and R. D. Borchardt (1985). Predicting relative ground response, Evaluating earthquake hazards in the Los Angeles region—an earth-sciences perspective, *U.S. Geol. Surv. Profess. Pap.* **1360**, 221–247.
- Sanders, C. O. and H. Kanamori (1984). A seismotectonic analysis of the Anza seismic gap, San Jacinto fault zone, southern California, *J. Geophys. Res.* **89**, 5873–5890.
- Seale, S. H. and R. J. Archuleta (1989). Site amplification and attenuation of strong ground motion, *Bull. Seism. Soc. Am.* **79**, 1673–1696.
- Seed, H. B. and I. M. Idriss (1970). Soil moduli and damping factors for dynamic response analysis, Report No. EERC 70-10, Earthquake Engineering Research Center, University of California, Berkeley, California.
- Sieh, K., M. Stuiver, and D. Brillinger (1989). A more precise chronology of earthquakes produced by the San Andreas fault in southern California, *J. Geophys. Res.* **94**, 603–623.
- Shearer, P. M. and J. A. Orcutt, (1987). Surface and near-surface effects on seismic waves—theory and borehole seismometer results, *Bull. Seism. Soc. Am.* **77**, 1168–1196.
- Silva, W. (1976). Body waves in a layered anelastic solid, *Bull. Seism. Soc. Am.* **66**, 1539–1554.
- Singh, S. K., E. Mena, and R. Castro (1988). Some aspects of source characteristics of the 19 September 1985 Michoacan earthquake and ground motion amplification in and near Mexico City from strong motion data, *Bull. Seism. Soc. Am.* **78**, 451–477.

- Sun, J. I., R. Golesorkhi and H. B. Seed (1988). Dynamic moduli and damping ratios for cohesive soils, Report No. UCB/EERC-88/15, Earthquake Engineering Research Center, University of California, Berkeley, California, 42 pp.
- Thatcher, W., J. A. Hileman, and T. C. Hanks (1975). Seismic slip distribution along the San Jacinto fault zone, southern California, and its implications, *Geol. Soc. Am. Bull.* **86**, 1140-1146.
- Vidal, A. and L. Munguía (1991). Local magnitude and source parameters for earthquakes in the Peninsular Ranges of Baja California, Mexico, *Bull. Seism. Soc. Am.* **81**, 2254-2267.

DEPARTMENT OF GEOLOGICAL SCIENCES
UNIVERSITY OF SANTA BARBARA
SANTA BARBARA, CALIFORNIA 93106-9630
(R.J.A.)

INSTITUTE FOR CRUSTAL STUDIES
UNIVERSITY OF CALIFORNIA, SANTA BARBARA
SANTA BARBARA, CALIFORNIA 93106-1100
(R.J.A., S.H.S., S.T.S.)

WARREN & SELBERT, INC.
222 E. CARRILLO STREET, SUITE 310
SANTA BARBARA, CALIFORNIA 93101
(P.V.S.)

U.S. GEOLOGICAL SURVEY
345 MIDDLEFIELD ROAD
MENLO PARK, CALIFORNIA 93101
(L.M.B.)

Manuscript received 2 August 1991